

# Clinopyroxene dissolution in basaltic melt

Yang Chen\*, Youxue Zhang

*Department of Geological Sciences, The University of Michigan, 2534 C.C. Little Building, 1100 North University Avenue,  
Ann Arbor, MI 48109-1005, USA*

Received 3 February 2009; accepted in revised form 17 June 2009; available online 24 June 2009

## Abstract

The history of magmatic systems may be inferred from reactions between mantle xenoliths and host basalt if the thermodynamics and kinetics of the reactions are quantified. To study diffusive and convective clinopyroxene dissolution in silicate melts, diffusive clinopyroxene dissolution experiments were conducted at 0.47–1.90 GPa and 1509–1790 K in a piston-cylinder apparatus. Clinopyroxene saturation is found to be roughly determined by MgO and CaO content. The effective binary diffusivities,  $D_{\text{MgO}}$  and  $D_{\text{CaO}}$ , and the interface melt saturation condition,  $C_0^{\text{MgO}} \times C_0^{\text{CaO}}$ , are extracted from the experiments.  $D_{\text{MgO}}$  and  $D_{\text{CaO}}$  show Arrhenian dependence on temperature. The pressure dependence is small and not resolved within 0.47–1.90 GPa.  $C_0^{\text{MgO}} \times C_0^{\text{CaO}}$  in the interface melt increases with increasing temperature, but decreases with increasing pressure. Convective clinopyroxene dissolution, where the convection is driven by the density difference between the crystal and melt, is modeled using the diffusivities and interface melt saturation condition. Previous studies showed that the convective dissolution rate depends on the thermodynamics, kinetics and fluid dynamics of the system. Comparing our results for clinopyroxene dissolution to results from a previous study on convective olivine dissolution shows that the kinetic and fluid dynamic aspects of the two minerals are quite similar. However, the thermodynamics of clinopyroxene dissolution depends more strongly on the degree of superheating and composition of the host melt than that of olivine dissolution. The models for clinopyroxene and olivine dissolution are tested against literature experiments on mineral–melt interaction. They are then applied to previously proposed reactions between Hawaii basalts and mantle minerals, mid-ocean ridge basalts and mantle minerals, and xenoliths digestion in a basalt at Kuandian, Northeast China.

© 2009 Elsevier Ltd. All rights reserved.

## 1. INTRODUCTION

Reactive textures are commonly found along the surface of mantle xenoliths. Dissolution or growth may happen depending on the saturation status of the xenolith minerals in the melt (Morgan and Liang, 2005; Shaw and Dingwell, 2008). The history of the xenolith–melt system may be inferred from the textures if the thermodynamic and kinetic aspects of the reactions are quantified. Clinopyroxene is a common mineral in mantle xenoliths, and hence an important component in the xenolith–melt reaction process.

Clinopyroxene is usually the main reservoir for incompatible elements in mantle rocks. For example, the partitioning coefficients of rare earth elements between clinopyroxene and melt are on the order of 0.1–0.01, 10 times higher than that of olivine and orthopyroxene. Clinopyroxene can contain high water content under certain conditions (Bell and Rossman, 1992; Gavrilenko and Keppler, 2007). Thus, clinopyroxene reactions with the host melt may affect trace element and volatile budgets.

Crystal dissolution in nature often occurs under convective conditions, where convection can be driven by the density difference between the crystal and melt, or the density difference between the interface melt and far-field melt (e.g., Kerr, 1995; Shaw, 2000). Theory on convective crystal dissolution has been developed by Kerr (1995) for Reynolds number  $\leq 1$ , and later expanded by Zhang and Xu (2003) to

\* Corresponding author.

E-mail addresses: [yangcz@umich.edu](mailto:yangcz@umich.edu) (Y. Chen), [youxue@umich.edu](mailto:youxue@umich.edu) (Y. Zhang).

Reynolds number up to  $10^5$ . This approach has been tested by halide dissolution in aqueous sodium carboxymethyl cellulose solutions (Kerr, 1995), halide dissolution in water (Zhang and Xu, 2003),  $\text{CO}_2$  droplet dissolution in seawater (Zhang, 2005), and  $\text{CO}_2$  bubble growth in beer (Zhang and Xu, 2008). Application of this theory requires two key parameters: the saturation condition (i.e., the interface melt composition at given  $T$  and  $P$ ) and the diffusivity in the host melt, both of which can be obtained by diffusive crystal dissolution experiments. Convective crystal dissolution experiments, on the other hand, cannot be used to quantify diffusivity. Furthermore, convective crystal dissolution experiments in laboratories often do not mimic the conditions of natural convective crystal dissolution, and the observed convective dissolution rate may not be applicable to natural conditions. Hence, the approach of this study is to carry out diffusive clinopyroxene dissolution experiments to understand both diffusive and convective clinopyroxene dissolution. The diffusivity and interface melt composition are obtained from the diffusive experiments and applied to convective crystal dissolution in nature.

Experimental studies on clinopyroxene dissolution are limited (Fig. 1). In the early experiments by Scarfe et al. (1980) and Brearley and Scarfe (1986) convection was not controlled and affected the dissolution process, causing inaccuracy in the derived diffusivities (Zhang et al., 1989). Kuo and Kirkpatrick (1985) studied diopside melting in its own melt at 1 atm and measured the interface reaction rate. Zhang et al. (1989) investigated diffusive diopside dissolution in an andesitic melt (3 sets of  $P$ – $T$  conditions) and highlighted past errors in extracting diffusivities from convective dissolution experiments. Van Orman and Grove (2000) studied diffusive diopside dissolution in a lunar ferrobasalt at four  $P$ – $T$  conditions but only reported diffusivities and interface melt composition at 1623 K and 1.3 GPa.

Hence, new and systematic diffusive dissolution experiments covering a wide range of  $P$  and  $T$  conditions are necessary to better quantify the diffusivity and saturation condition, in order to model convective clinopyroxene dissolution.

In this study, we investigate non-convective clinopyroxene dissolution in basalt at 0.47–1.90 GPa and 1509–1790 K. This is a sister study of our recent work on olivine dissolution in basalt (Chen and Zhang, 2008). Convective clinopyroxene dissolution is then modeled using the interface melt composition and diffusivities extracted from the experiments. This model and the previous model on olivine dissolution are applied to mineral–melt reactions in Hawaii basalts, mid-Atlantic ridge basalts, and continental intra-plate basalts at Kuandian, Northeast China.

## 2. EXPERIMENTS AND ANALYTICAL METHODS

A clinopyroxene crystal and a basaltic glass disc are placed together and heated to above the liquidus of the basalt in a 1/2-inch piston-cylinder apparatus. The basaltic glass was from Juan de Fuca Ridge (Dixon et al., 1986, 1988). Its composition is listed in Table 1. Tholeiitic basalt glass was chosen because tholeiite is the most common basalt and natural glass samples are available. The glass was cut and ground into 2 mm diameter rods and sliced into  $\sim 1.6$  mm thick discs, and doubly polished. The clinopyroxene is a natural sample from American Museum of Natural History. Its composition is close to diopside end-member (Table 1). The clinopyroxene crystal was cut and ground into  $\sim 2.4$  mm diameter rods and sliced into  $\sim 1.1$  mm thick discs, and doubly polished. The clinopyroxene is difficult to machine because it breaks easily along its cleavages. Efforts were made to minimize cracks in the clinopyroxene discs used in experiments, but minor cracks were difficult to avoid.

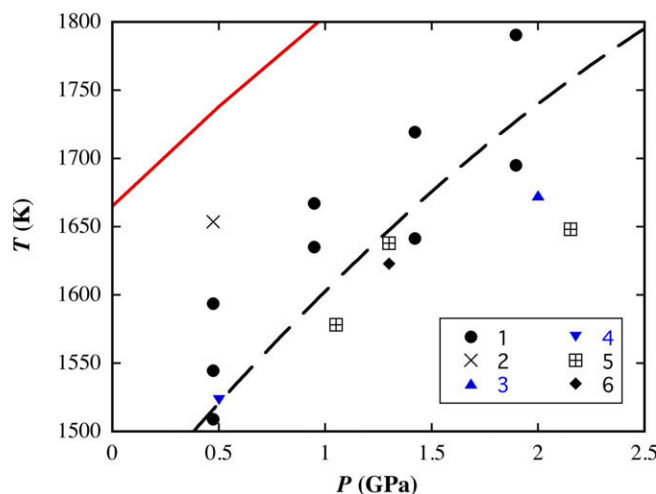


Fig. 1.  $T$  and  $P$  conditions of clinopyroxene dissolution experiments. Data sources: 1. This study (50 wt%  $\text{SiO}_2$  in the melt); 2. A failed experiment of this study, in which the clinopyroxene partially melted; 3. Scarfe et al. (1980), convective clinopyroxene dissolution in alkali basalt (47 wt%  $\text{SiO}_2$ ); 4. Brearley and Scarfe (1986), clinopyroxene dissolution in alkali basalt (49 wt%  $\text{SiO}_2$ ); 5. Zhang et al. (1989), diffusive diopside dissolution in andesite (56 wt%  $\text{SiO}_2$ ); 6. Van Orman and Grove (2000), diffusive diopside dissolution in lunar ferrobasalt (47 wt%  $\text{SiO}_2$ ). The solid curve is the pure diopside melting curve by Boyd and England (1963) and Williams and Kennedy (1969). The dashed curve is the rough liquidus of the basalt used in this study, estimated by MELTS program (Ghiorso and Sack, 1995; Asimow and Ghiorso, 1998).

Table 1  
Starting clinopyroxene and glass composition (wt%).

	Clinopyroxene	Basalt	Electron microprobe analysis <sup>a</sup>	
			2 $\sigma$ Error	Standard
SiO <sub>2</sub>	54.15	50.23	0.40	K-feldspar
TiO <sub>2</sub>		1.94	0.08	Geikielite
Al <sub>2</sub> O <sub>3</sub>	0.60	13.61	0.16	K-feldspar
FeO	0.91	12.06	0.19	Ferrosilite
MnO		0.22	0.11	Rhodonite
MgO	17.90	7.05	0.12	Olivine
CaO	25.40	10.75	0.19	Clinopyroxene
Na <sub>2</sub> O	0.41	2.73	0.10	Albite
K <sub>2</sub> O		0.17	0.05	K-feldspar
P <sub>2</sub> O <sub>5</sub>		0.10	0.09	Apatite
H <sub>2</sub> O		0.25–0.40 <sup>b</sup>		
Total	99.37	99.16		

<sup>a</sup> Beam condition: 15 kV, 5 nA, 5 × 5 or 20 × 20  $\mu$ m raster. Counting time: 60 s for SiO<sub>2</sub> and FeO, 30 s for TiO<sub>2</sub> and CaO, and 20 s for the others.

<sup>b</sup> Fourier transform infrared spectrometry measurement.

The sample assembly follows the design in [Chen and Zhang \(2008\)](#). The interface melt produced by clinopyroxene is actually less dense than the initial basaltic melt, based on the density model of [Lange and Carmichael \(1987\)](#) and [Ochs and Lange \(1999\)](#). This was not realized until Exp# 1, 5, 6 and 7 were done. Hence, in Exp# 1, 5, 6 and 7, the clinopyroxene disc was placed under the glass disc, while in later experiments it was placed on the top to prevent convection. The potential problem of convection in Exp# 1, 5, 6 and 7 will be evaluated in Section 3.

The experimental procedure follows [Chen and Zhang \(2008\)](#). [Chen and Zhang \(2008\)](#) carried out time-series experiments on olivine dissolution to examine how the interface melt composition and the compositional profile in the melt evolve with experimental duration. They concluded that the interface reaction was rapid for olivine dissolution. Time-series experiments were not conducted in this study because (1) the clinopyroxene–melt interface reaction is more rapid than olivine–melt interface reaction rate ([Kuo and Kirkpatrick, 1985](#)); (2) [Zhang et al. \(1989\)](#) showed that interface reaction is so rapid that diffusion takes control within 0.0002–0.2 s; and (3) our experimental design is proved to suppress convection effectively ([Zhang et al., 1989](#); [Chen and Zhang, 2008](#)). The duration of the experiments is designed to be long enough to generate a measurable diffusion profile, but short enough so that the melt can be treated as an infinite reservoir.

Nine experiments were conducted at  $T$  and  $P$  shown in [Fig. 1](#). The feasible  $T$ – $P$  conditions are limited by two factors. First, the temperature must be higher than the liquidus temperature of the basalt, otherwise crystallization occurs. Based on MELTS program ([Ghiorso and Sack, 1995](#); [Asimow and Ghiorso, 1998](#)), the liquidus phase is olivine at low pressure and clinopyroxene at high pressure. Crystallization in the bulk melt must be avoided because it disturbs the diffusion and dissolution processes. Second, the temperature must be lower than the melting temperature of the clinopyroxene. At 0.47 GPa, the melting point for pure

diopside is ~1733 K ([Boyd and England, 1963](#); [Williams and Kennedy, 1969](#)), but the clinopyroxene used in this study is not a pure diopside and was partially melted at 1653 K (the failed experiment in [Fig. 1](#)). The suitable temperature range at a given pressure is limited to a window of ~200 K by these two factors. Considering that the predictions by MELTS program have some errors, experiments were tried at temperatures slightly lower than the liquidus predicted by MELTS program in order to better constrain the temperature dependence of the diffusivities and interface melt saturation condition. It turned out that no crystallization occurred at ~30 K below the predicted liquidus.

After the experiments, the samples were examined under electron microprobe. Compositional profiles in the glass were measured. The analytical details are in [Table 1](#).

### 3. EXPERIMENTAL RESULTS

[Table 2](#) shows the run conditions of all successful experiments. [Fig. 2](#) shows a BSE image of a polished experimental charge and an associated MgO concentration profile. The large center part of the clinopyroxene crystal is in contact with the melt and was dissolved and indented. Since the clinopyroxene disc has a larger diameter than the glass disc, the narrow rim part of the clinopyroxene remains intact. The clinopyroxene crystal and glass are always cracked after exposure. The cracks in glass are sub-parallel to the clinopyroxene–glass interface and are unfilled, indicating that they formed during quench. Cracks in clinopyroxene crystals are unfilled, filled by graphite, or filled by glass. The cracks filled by glass are avoided when measuring compositional profiles.

The interface between clinopyroxene and melt is not as flat ([Figs. 3a, Fig. 4a](#)) as that between olivine and melt in [Chen and Zhang \(2008\)](#). Examining the clinopyroxene–melt interface under optical microscope shows that when a cleavage intersects the interface, the interface indents ([Fig. 4b](#)). Every major indentation is correlated with a major cleavage in the clinopyroxene. Those major indentations are avoided in measuring dissolution distance and compositional profiles.

Quench crystals are observed in all experiments. They fall into two categories based on their morphology and experimental conditions. At temperatures lower than 1544 K (Exp# 1 and 14), a few needle-shaped or dendritic crystals (<10  $\mu$ m long) extend from the interface into the glass ([Fig. 3a](#)). At temperatures higher than 1544 K, clusters of crystals with dendritic texture extend up to 270  $\mu$ m away from the interface ([Fig. 3b](#)). Crystals of both types are attached to the crystal–melt interface. No crystals are found in other regions in the glass. The composition of the crystals cannot be measured accurately because they are too thin. EDS analyses suggest they are clinopyroxenes. The compositional profiles within the crystalline zone were measured with 20 × 20  $\mu$ m electron beam size, as opposed to 5 × 5  $\mu$ m used for crystal-free zone.

Clinopyroxene dissolution distance is directly measured in three ways ( $L_1$ ,  $L_2$  and  $L_3$  in [Table 2](#)).  $L_1$  is obtained by subtracting the final clinopyroxene thickness (measured under optical microscope) from the initial thickness (measured by a digital micrometer).  $L_2$  is the dissolution distance

Table 2  
Summary of experimental conditions and dissolution distances.

Exp#	$T_1$ (K)	$T_2$ (K)	$P$ (GPa)	Duration (s)		Diopside dissolution distance ( $\mu\text{m}$ )			
				$t_1$	$t_2$	$L_1^a$	$L_2$	$L_3$	$L_4$
1	1544	1555	0.47	1799	1807	$37 \pm 10$	$37 \pm 6$	$38 \pm 6$	$31 \pm 2$
5	1635	1654	0.95	725	732	$<81$	$49 \pm 16$	$50 \pm 15$	$51 \pm 3$
6	1719	1743	1.42	720	732	$<198$	$158 \pm 7$	$155 \pm 6$	$163 \pm 4$
7	1594	1624	0.47	605	613	$<89$	$67 \pm 8$	$65 \pm 7$	$94 \pm 10$
8	1667	1694	0.95	721	733	$<247$	$138 \pm 10$	$138 \pm 9$	$141 \pm 6$
11	1695	1748	1.90	482	494	$<92$	$44 \pm 13$	$44 \pm 12$	$41 \pm 3$
12	1641	1680	1.42	721	732	$<118$	$31 \pm 13$	$30 \pm 12$	$28 \pm 2$
14	1509	1517	0.47	2397	2404	$<22$	$11 \pm 10$	$7 \pm 9$	$8 \pm 1$
15 <sup>b</sup>	1790	1797	1.90	356	378	$<236$			$147 \pm 8$

Note:  $T_1$  is corrected experimental temperature (Hui et al., 2008).  $T_2$  is the liquidus temperature of the interface melt calculated using MELTS program (interface melt compositions are listed in Table 4).  $P$  is the corrected pressure.  $t_1$  is the nominal duration.  $t_2$  is the corrected duration.  $L_1$  is obtained by subtracting the final clinopyroxene thickness (measured under optical microscope) from the initial thickness (using a digital micrometer).  $L_2$  is the dissolution distance measured under optical microscope using the clinopyroxene rim as a reference.  $L_3$  is that measured under electron microprobe.  $L_4$  is calculated by Eq. (5). The errors are at  $2\sigma$  level.

All experiments except for Exp# 15 were heated up by single stage of fixed heating rate of 900 K/min. Exp# 15 was conducted in a different piston-cylinder apparatus. Type-D thermocouple was used instead of type-S. The sample was heated up through multiple stages of different heating rates to minimize temperature overshooting.

<sup>a</sup> For most experiments a small melt reservoir existed on the other side of the clinopyroxene disc opposite to the major melt reservoir, and consumed some clinopyroxene. Hence  $L_1$  values for most experiments are only upper limits.

<sup>b</sup> The rim of the clinopyroxene crystal in the cross section of Exp# 15 is dissolved, hence  $L_2$  and  $L_3$  are not measured.

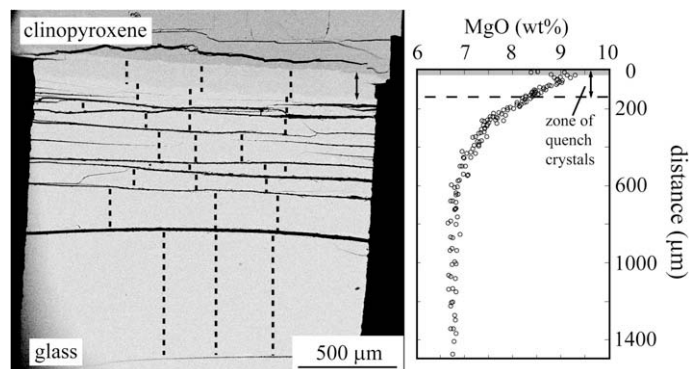


Fig. 2. Back-scattered electron image of the cross-section of Exp# 11 and corresponding MgO concentration profile measured by electron microprobe. In the BSE image, the clinopyroxene disc is on top of the basaltic glass cylinder. Electron microprobe analysis traverses are shown as dashed lines. An enlarged view of the zone of quench crystals is shown in Fig. 3b. In the profile (right-hand side), the MgO concentration increases towards the clinopyroxene–melt interface, but decreases abruptly at very close to the interface (at distance of 0–20  $\mu\text{m}$ , marked by the shaded zone). Note that the zone of quench crystals extends beyond this shaded zone, and the profile segment within the zone of quench crystals connects smoothly with the profile segment farther away from the interface.

measured under optical microscope using the clinopyroxene rim as a reference.  $L_3$  is that measured under electron microprobe. Measurement of the final clinopyroxene thickness under microscope has an error of  $\pm 5 \mu\text{m}$ . Measurement of the dissolution distance between the rim and the center has a reading error of  $\pm 1.25 \mu\text{m}$  under microscope, and  $\pm 0.5 \mu\text{m}$  under electron microprobe. A more important source of error is the heterogeneity in the initial clinopyroxene thickness, which on average is about  $\pm 9 \mu\text{m}$  ( $2\sigma$ ). The heterogeneity is caused mainly by two factors: (1) the rim tends to be thinner than the center; (2) when a crack intersects the surface, the adjacent area tends to be thinner.

Compositional profiles of Exp# 1 are shown in Fig. 5. The profiles of the other experiments and data of all

experiments are in Electronic Annex 1 and 2, respectively. For each experiment multiple compositional traverses were measured. The traverses match suggesting that they were not disturbed by convection (e.g., Shaw, 2000). The profiles can be fitted well with Eq. (2a) (Section 4.2). The diffusivities and interface melt compositions extracted from Exp# 1, 5, 6 and 7, in which the crystal disc was placed below the glass disc, are consistent with later experiments (Sections 4.2 and 4.3). If convection occurred in these early experiments, there would be systematic differences between the experimental datasets. Furthermore, the stability of the melt boundary layer regarding composition-driven convection can be evaluated by estimating its compositional Rayleigh number:

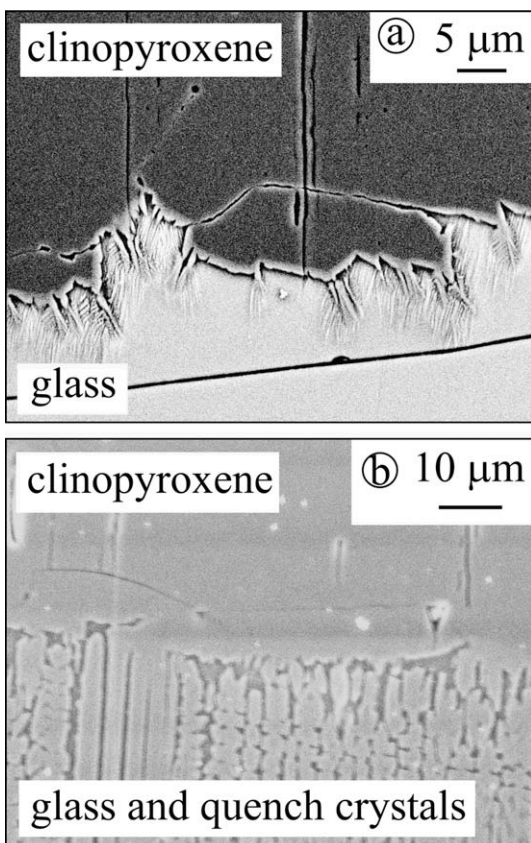


Fig. 3. BSE images of two different types of quench crystal morphology. (a) In a low temperature experiment (Exp# 1, 1544 K). (b) In a high temperature experiment (Exp# 11, 1695 K).

$$Ra = \frac{g\Delta\rho d^3}{\eta D}, \quad (1)$$

where  $g$  is the gravity constant,  $\Delta\rho$  is the density difference,  $d$  is the boundary layer thickness,  $\eta$  is the melt viscosity, and  $D$  is the diffusivity. This value must exceed about 1000 for the boundary layer to be unstable (Sparks et al., 1984). In Exp# 1, 5, 6 and 7, the boundary layer is not thick enough to satisfy this criterion.

The compositional profiles in the far-field are flat. The far-field melt compositions agree well with the initial composition. In general,  $\text{SiO}_2$ ,  $\text{MgO}$  and  $\text{CaO}$  increase towards the clinopyroxene–melt interface, while the other components decrease. These general trends change abruptly at very close to the clinopyroxene–melt interface:  $\text{SiO}_2$ ,  $\text{MgO}$  and  $\text{CaO}$  decrease (e.g., the  $\text{MgO}$  profile in Fig. 2 marked by the shaded zone) while  $\text{TiO}_2$ ,  $\text{Al}_2\text{O}_3$ ,  $\text{FeO}$ ,  $\text{Na}_2\text{O}$  and  $\text{K}_2\text{O}$  increase when approaching the interface. This bend of the profiles has been observed previously (e.g., Zhang et al., 1989; Chen and Zhang, 2008) and is attributed to clinopyroxene overgrowth during quench (see Section 4.1). Note that this feature is not clearly resolved in some experiments (e.g., Exp# 1 in Fig. 5).  $\text{FeO}$  shows uphill diffusion toward the interface in Exp# 1, 12 and 14, but in other experiments the uphill diffusion is not obvious.

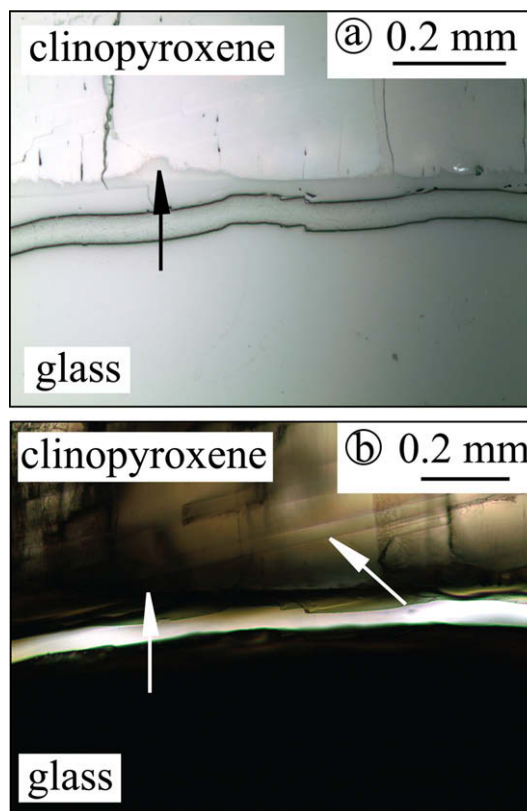


Fig. 4. Optical microscope images of Exp# 1. (a) Reflective light. Black arrow points to a major indentation in the interface. (b) Transmitted light on the same area in (a). The white arrow on the left points to the position of the major indentation shown in (a). The white arrow on the right points to a cleavage that intersects the interface at the position of the indentation.

## 4. DISCUSSION AND APPLICATIONS

### 4.1. Interface crystals and quench effect

Although the melt near the interface contains numerous tiny crystals, the compositional profiles in this zone (averaged by  $20 \times 20 \mu\text{m}$  electron beam) agree with those in the crystal-free zone (Fig. 2), suggesting that they are not disturbed by the crystals. This consistency and the dendritic texture of the crystals suggest that the crystals formed during quench, not during clinopyroxene dissolution.

The bent profiles very close to the interface (the shaded zone of the profile in Fig. 2) are attributed to clinopyroxene overgrowth on the existing crystal surface during quench. The exact composition of the overgrowing clinopyroxene cannot be measured because the layer is too thin. MELTS program suggests that Mg- and Ca-rich clinopyroxene is the liquidus phase of the interface melt, which is expected because the interface melt is close to the saturation of Mg- and Ca-rich clinopyroxene. Growth of such an Mg- and Ca-rich clinopyroxene on the existing crystal surface during quench would cause the depletions of  $\text{SiO}_2$ ,  $\text{MgO}$  and  $\text{CaO}$  in the interface melt. The bent profiles are not clearly resolved in some experiments, and are less

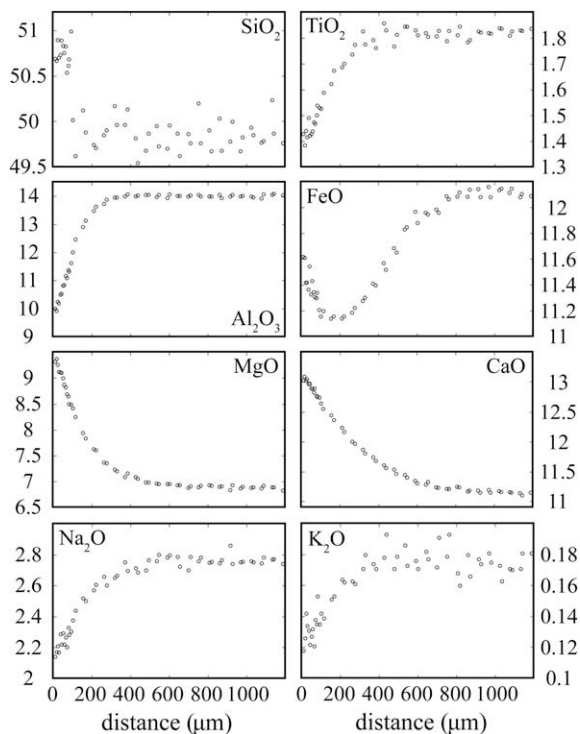


Fig. 5. Compositional profiles in the quenched glass of Exp# 1 (1544 K, 0.47 GPa, 30 min). The vertical axes are oxide concentrations in wt%. The horizontal axis is the distance to the clinopyroxene–glass interface.

significant compared to the feature in olivine dissolution experiments (Chen and Zhang, 2008). This may be explained by smaller compositional difference between clinopyroxene and melt than between olivine and melt. It is interesting to see that the extent of the quench crystals does not match the length of the bent profiles.

In summary, there are two quench effects: the first is the dendritic growth of clinopyroxene crystals in the melt near the interface; and the second is the uniform overgrowth of clinopyroxene on the existing clinopyroxene surface. For the first quench effect, the melt composition before the dendritic growth can be recovered by using large beam size in electron microprobe analyses, and are not excluded when the profiles are treated to quantify the diffusivity and interface melt composition (Section 4.2). The bent part of the profile is caused by the second quench effect and not related to clinopyroxene dissolution. It is therefore excluded when the profiles are treated.

#### 4.2. Profile treatment and effective binary diffusivity

The main purpose of the experiments is to obtain the interface melt composition and diffusivities. There is some concern that the diffusivities in the melt could not be determined because clinopyroxene is a solid solution and diffusion in clinopyroxene might control the dissolution kinetics. Liang (2000) studied the effect of solid solution on crystal dissolution and concluded that dissolution of practically all minerals in natural melts is controlled by diffusion in the melt, meaning that the diffusion in clinopy-

roxene does not affect the dissolution rate. Hence, the compositional profiles in the melt can be fitted by the solution to the one-dimensional diffusive dissolution equation (Crank, 1975; Zhang et al., 1989; Liang, 1999) to obtain effective binary diffusivities:

$$C = C_{\infty} + (C_0 - C_{\infty}) \frac{\operatorname{erfc}\left(\frac{x}{2\sqrt{Dt}} - \alpha\right)}{\operatorname{erfc}(-\alpha)} \quad (2a)$$

where  $C$  is the component concentration in the melt,  $C_0$  is the concentration at the crystal–melt interface,  $C_{\infty}$  is the concentration at far-field, and should be a constant for the solution to be valid,  $x$  is the distance to the crystal–melt interface,  $D$  is the effective binary diffusivity of the component,  $t$  is the duration of the experiment, and  $\alpha$  satisfies:

$$\exp(\alpha^2) \operatorname{erfc}(-\alpha) \sqrt{\pi} \alpha = \frac{C_0 - C_{\infty}}{C_c - C_0}, \quad (2b)$$

where  $C_c$  is the concentration of the component in the crystal. The crystal dissolution distance  $L$  can be expressed as:

$$L = 2\alpha \frac{\rho_m}{\rho_c} \sqrt{Dt}, \quad (2c)$$

where  $\rho_m$  and  $\rho_c$  are the density of the melt and crystal, respectively.

Fitting a profile by Eqs. (2a) and (2b) yields  $C_0$ ,  $C_{\infty}$  and  $D$  of the component. The results are substituted in Eq. (2c) and the calculated crystal dissolution distance is compared with the  $L_1$ ,  $L_2$  and  $L_3$  (Table 2). This calculation is independent of the direct measurements and provides cross-check on the quality of the experiments.

The bent profiles close to the interface are excluded for profile fitting. The length of the excluded part is set as  $4\left(\int_{t_0}^{t_1} D dt\right)^{1/2}$ , where  $t_0$  is the time when the power is turned off, and  $t_1$  is the time when the sample reaches room temperature. The excluded parts vary from  $\sim 16 \mu\text{m}$  in  $\sim 1509 \text{ K}$  experiments to  $\sim 50 \mu\text{m}$  in  $\sim 1790 \text{ K}$  experiments. The apparent concentration maxima of MgO and CaO profiles always lie within the excluded segment.

Experimental durations are corrected for the effect of heating up and quenching following Zhang and Behrens (2000). The corrections are  $\sim 7$ – $12 \text{ s}$  for Exp# 1–14, and  $22 \text{ s}$  for Exp# 15 (Table 2). The maximum correction amounts to 6% increase in the effective experimental duration.

The profiles for  $\text{SiO}_2$ ,  $\text{TiO}_2$ ,  $\text{Al}_2\text{O}_3$ , MgO, CaO and  $\text{Na}_2\text{O}$  have been fitted (Electronic Annex 1). The effective binary diffusivities are listed in Table 3.  $\text{SiO}_2$  profiles of Exp# 1, 12, 14 are not fitted because the profiles do not constrain the diffusivity well. FeO profiles show uphill diffusion and cannot be treated by the effective binary diffusion approach. In the fitting results  $D_{\text{CaO}}$  is the highest and  $D_{\text{SiO}_2}$  is the lowest. Using  $D_{\text{MgO}}$  as reference,  $D_{\text{SiO}_2} \approx 0.48 D_{\text{MgO}}$ ,  $D_{\text{TiO}_2} \approx 0.8 D_{\text{MgO}}$ ,  $D_{\text{Al}_2\text{O}_3} \approx 0.56 D_{\text{MgO}}$ ,  $D_{\text{CaO}} \approx 2.4 D_{\text{MgO}}$ , and  $D_{\text{Na}_2\text{O}} \approx 1.3 D_{\text{MgO}}$ . The fact that  $\text{Na}_2\text{O}$  diffuses slower than CaO suggests complicated multi-component effect (e.g., Zhang et al., 1989). The diffusivities of different components tend to converge as temperature increases, but do not converge at the same temperature (there is no single compensation temperature).

Table 3  
Effective binary diffusivities with  $2\sigma$  fitting errors ( $\mu\text{m}^2/\text{s}$ ).

Exp#	SiO <sub>2</sub>		TiO <sub>2</sub>		Al <sub>2</sub> O <sub>3</sub>		MgO		CaO		Na <sub>2</sub> O	
	<i>D</i>	$2\sigma$	<i>D</i>	$2\sigma$	<i>D</i>	$2\sigma$	<i>D</i>	$2\sigma$	<i>D</i>	$2\sigma$	<i>D</i>	$2\sigma$
1	ND		8.1	1.6	3.8	0.3	8.9	0.7	29.7	1.6	9.9	2.1
5	5.4	0.9	16.1	1.4	10.0	0.4	24.0	1.4	52.9	3.0	28.9	2.9
6	46.4	7.1	49.2	2.5	45.1	1.0	72.3	2.0	134.1	4.2	94.7	5.4
7	6.6	1.1	17.2	1.2	10.4	0.6	18.8	1.5	56.2	4.0	34.4	3.2
8	24.7	3.1	30.7	1.9	19.3	0.6	35.0	1.0	81.5	3.3	55.8	3.7
11	29.3	10.6	92.0	15.8	35.5	2.4	59.2	4.3	84.4	6.2	67.9	10.1
12	ND		17.1	5.8	16.1	1.5	28.2	2.5	69.4	6.0	37.7	9.6
14	ND		6.4	3.0	4.3	0.8	6.3	1.2	20.2	2.8	ND	
15	50.4	5.8	62.2	10.8	71.6	2.0	111.9	3.0	197.4	9.6	123.6	9.1

ND: Not determined because the profile does not constrain the diffusivity well.

$D_{\text{MgO}}$  and  $D_{\text{CaO}}$  as functions of temperature are shown in Fig. 6. The temperature dependence is well described by the Arrhenian relation. The pressure dependence of the diffusivities at 0.47–1.9 GPa is small and not resolved.  $D_{\text{MgO}}$  and  $D_{\text{CaO}}$  are modeled as:

$$\ln D_{\text{MgO}} = -6.664(\pm 0.745) - \frac{28897(\pm 1221)}{T}, \quad (3a)$$

and

$$\ln D_{\text{CaO}} = -10.517(\pm 0.901) - \frac{21205(\pm 1476)}{T} \quad (3b)$$

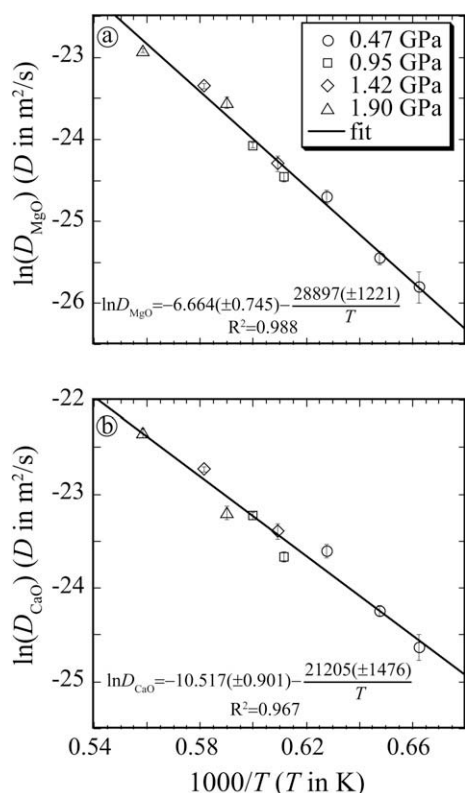


Fig. 6. Effective binary diffusivities of MgO and CaO in the basaltic melt as functions of  $T$ . The diffusivities are obtained by fitting the compositional profiles with Eq. (2). The error bars represent  $2\sigma$  fitting errors.

where the diffusivities are in  $\text{m}^2/\text{s}$  and  $T$  is in K. The errors given hereafter are at  $2\sigma$  level. The activation energy is  $240 \pm 20$  and  $176 \pm 25$  kJ/mol for MgO and CaO, respectively. Eq. (3a) can reproduce  $D_{\text{MgO}}$  within 0.09 natural logarithm units. Eq. (3b) can reproduce  $D_{\text{CaO}}$  within 0.17 natural logarithm units.

The above equations are based on clinopyroxene dissolution in basalt and can be applied to MgO and CaO diffusion in similar melt compositions and concentration gradients. Although tholeiitic basalt is used in this study, the results can be applied to alkali basalt because the diffusivity in these two types of silicate melts fall within the corresponding errors (Chen and Zhang, 2008). Comparison with literature data shows that the effective binary diffusivities depend on the SiO<sub>2</sub> concentrations (Fig. 7). Applying the results to andesite will introduce some errors. Note that the data in Baker (1990), Kubicki et al. (1990) and Kress and Ghiorso (1995) are from diffusion couple experiments, not crystal dissolution experiments.

#### 4.3. Interface and far-field melt compositions

The interface melt compositions are listed in Table 4 and the far-field melt composition is in Table A1 (Electronic Annex 1). Where the profile for a component is not fitted with Eq. (2), its concentration in the interface melt is estimated by visual extrapolation of the profiles to  $x=0$  (excluding the bent part), and its concentration in the far-field melt is obtained by averaging the concentrations of the flat part of the far-field profile.

The far-field melt needs to be examined to verify that it was not affected by diffusion, so that Eq. (2) is applicable. The far-field profiles are flat, and the composition agrees with the initial composition. Therefore, diffusion did not affect the far-field melt. Small variation in the far-field melt composition is attributed to heterogeneity in the natural basaltic glass.

The interface melt composition is one critical parameter in modeling convective crystal dissolution and needs to be quantified. In this section the interface melt is treated as clinopyroxene saturated. However, the interface melt cannot be at exact saturation, because at exact saturation there would be neither dissolution nor growth. Nonetheless, based on the interface reaction rate by Kuo and Kirkpatrick (1985),

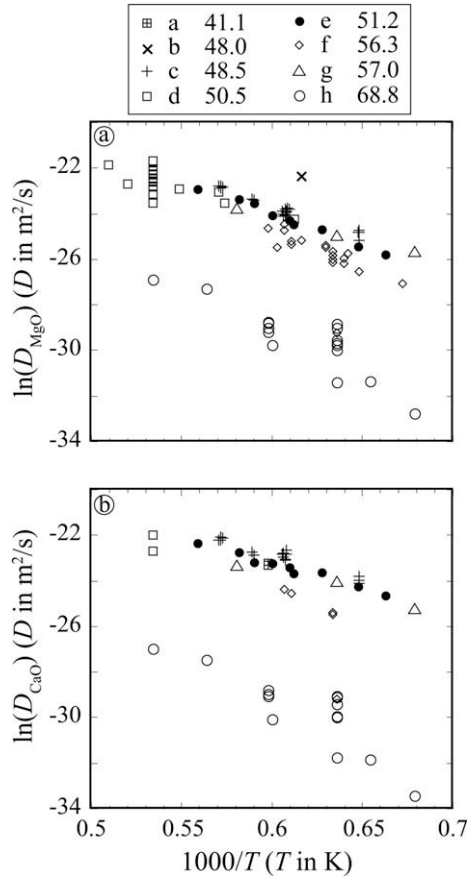


Fig. 7.  $D_{\text{MgO}}$  and  $D_{\text{CaO}}$  in silicate melts. The average  $\text{SiO}_2$  concentration of the silicate melts are listed in the legend. Data sources: (a) Morgan et al. (2006), anorthosite dissolution at 1673 K and 0.6 GPa; (b) Van Orman and Grove (2000), diopside dissolution at 1623 K and 1.3 GPa; (c) Chen and Zhang (2008), olivine dissolution at 1543–1753 K and 0.47–1.42 GPa; (d) Kubicki et al. (1990), diffusion couple at 1633–1873 K and 0.0001–2 GPa; (e) this study; (f) Zhang et al. (1989), olivine, diopside and quartz dissolution at 1488–1673 K and 0.5–2.15 GPa; (g) Kress and Ghiorso (1995), diffusion couple at 1473–1723 K and 0.0001 GPa; (h) Baker (1990), diffusion couple at 1473–1873 K and 0.0001–1 GPa. Note that the quartz dissolution experiment by Zhang et al. (1989) produced  $\text{SiO}_2$ -rich melt, such that the data point falls in the range of dacite and rhyolite.

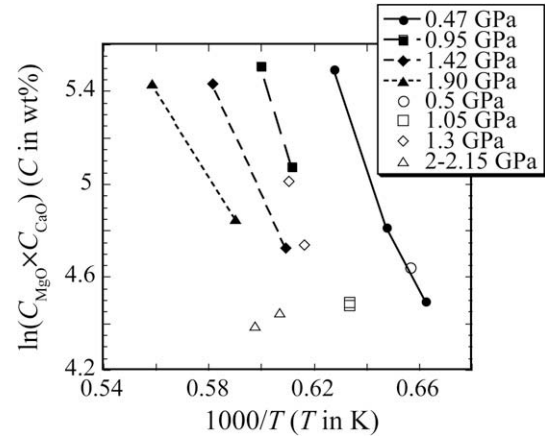


Fig. 8.  $C_{\text{MgO}} \times C_{\text{CaO}}$  of the interface melt at different  $P$  and  $T$ . Solid symbols are data from this study. Hollow symbols are literature data.  $\text{SiO}_2$  ranges from 47 to 56 wt%. See Fig. 1 for the experimental conditions of the literature data.

Zhang et al. (1989) showed that during clinopyroxene dissolution the interface melt reaches 99% of saturation within 0.0002–0.2 s. Hence, the interface melt is practically saturated with clinopyroxene considering the electron microprobe precision of no better than  $\sim 1\%$  relative. Another issue is that the saturation melt during diopside dissolution may not be the perfect equilibrium composition between the crystal and the melt if the crystal is a solid solution (Zhang et al., 1989; Liang, 2000; Zhang, 2008). That is, the saturation condition we derive below is best applied to clinopyroxene dissolution rather than clinopyroxene growth.

The saturation of Mg- and Ca-rich clinopyroxene may be determined by the three major components MgO, CaO and  $\text{SiO}_2$ . Putirka (1999) used two empirical expressions for diopside-melt equilibrium, involving either  $C_0^{\text{MgO}} \times C_0^{\text{CaO}} \times (C_0^{\text{SiO}_2})^2$  or  $C_0^{\text{CaO}} \times (C_0^{\text{SiO}_2})^2$ . These expressions and  $C_0^{\text{MgO}} \times C_0^{\text{CaO}}$  were tried in modeling the interface melt composition. Note that weight percent is used in this study instead of mole fraction for simplicity. Available experimental data do not show consistent trends in  $C_0^{\text{CaO}} \times (C_0^{\text{SiO}_2})^2$  versus  $T$  and  $P$ . At a given  $P$ ,  $C_0^{\text{MgO}} \times C_0^{\text{CaO}}$  versus  $1/T$  is roughly linear

Table 4  
Interface melt composition with  $2\sigma$  fitting errors (wt%).

Exp#	SiO <sub>2</sub>	TiO <sub>2</sub>	Al <sub>2</sub> O <sub>3</sub>	FeO <sup>b</sup>	MgO	CaO	Na <sub>2</sub> O						
1	51.21 <sup>c</sup>	1.37	0.02	9.57	0.10	11.6	9.40	0.05	13.12	0.02	2.14	0.03	
5	52.73	0.33	1.07	0.03	7.10	0.14	10.5	10.92	0.08	14.64	0.06	1.85	0.03
6	52.81	0.23	0.69	0.02	5.08	0.08	8.5	13.13	0.06	17.40	0.06	1.40	0.03
7	53.05	0.26	0.62	0.03	3.71	0.26	8.7	13.84	0.21	17.58	0.14	1.39	0.05
8	53.78	0.33	0.52	0.04	3.40	0.22	8.5	13.98	0.12	17.66	0.11	1.25	0.05
11	51.54	0.30	1.42	0.02	10.10	0.10	10.7	9.31	0.06	13.68	0.06	2.06	0.03
12	50.95 <sup>c</sup>		1.36	0.05	10.86	0.14	11.2	8.78	0.07	12.84	0.05	2.23	0.04
14	50.50 <sup>c</sup>		1.66	0.02	12.50	0.09	12.0	7.64	0.04	11.71	0.02	2.54	0.03
15	53.51	0.34	0.68	0.12	5.31	0.17	8.5	12.87	0.09	17.77	0.15	1.28	0.07

<sup>a</sup> MnO is  $\sim 0.2$  wt%, K<sub>2</sub>O and P<sub>2</sub>O<sub>5</sub> are  $\sim 0.1$  wt%.

<sup>b</sup> FeO profiles are not fitted. The interface FeO concentrations are estimated visually.

<sup>c</sup>  $\text{SiO}_2$  profiles of these experiments were not treated. The  $\text{SiO}_2$  concentrations are estimated visually.

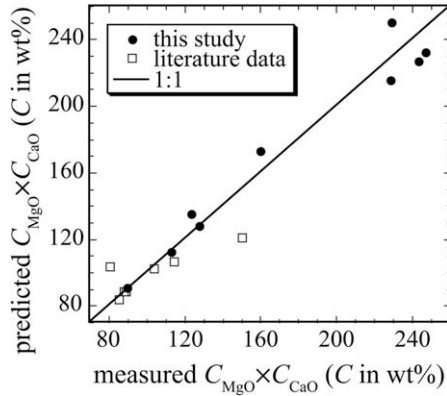


Fig. 9. Comparison between the prediction by Eq. (4) and the measured values. The  $2\sigma$  error in using Eq. (4) to predict  $\ln(C_0^{\text{MgO}} \times C_0^{\text{CaO}})$  is 0.11.

(Fig. 8), but  $C_0^{\text{MgO}} \times C_0^{\text{CaO}} \times (C_0^{\text{SiO}_2})^2$  versus  $1/T$  is strongly nonlinear. Even though it is theoretically more appealing to include  $(C_0^{\text{SiO}_2})^2$ , doing so would bring more complexity (handling highly nonlinear relations) with no improvement in data fitting. Therefore,  $C_0^{\text{MgO}} \times C_0^{\text{CaO}}$  is adopted in this study. The role of  $\text{SiO}_2$  is difficult to pin down from the available data.

Fig. 8 shows the dependence of  $C_0^{\text{MgO}} \times C_0^{\text{CaO}}$  on  $T$  and  $P$ .  $C_0^{\text{MgO}} \times C_0^{\text{CaO}}$  increases with increasing temperature, and decreases with increasing pressure.  $C_0^{\text{MgO}} \times C_0^{\text{CaO}}$  is modeled as:

$$\ln(C_0^{\text{MgO}} \times C_0^{\text{CaO}}) = 22.85(\pm 1.82) - 2.10(\pm 0.44)P - \frac{26360(\pm 2565)}{T} \pm 1.22(\pm 0.43) \times 10^6 \frac{P^2}{T^2}, \quad (4)$$

where  $C_0$  is in wt%,  $P$  is in GPa, and  $T$  is in K. The multiple linear correlation coefficient  $r$  is 0.9907. Two data points shown in Fig. 8 are not used in the regression because they deviate from the trend constrained by the other data. Eq. (4) is calibrated on the clinopyroxene dissolution experiments in basalt (including tholeiitic and alkali basalt) and andesite, and is readily applicable in this melt composition range. It has second-order terms of  $T$  and  $P$  and should not be extrapolated beyond the  $T$  and  $P$  range of the data (Fig. 1). Extrapolating to lower pressures may be safe because the second-order term diminishes as  $P$  approaches zero. Fig. 9 shows the prediction by this formula compared to the data. The  $2\sigma$  error in using Eq. (4) to predict  $\ln(C_{\text{MgO}} \times C_{\text{CaO}})$  is 0.11. The  $2\sigma$  errors in predicting  $C_0^{\text{MgO}}$  and  $C_0^{\text{CaO}}$  are 1.2 wt% and 1.5 wt%, respectively.

#### 4.4. Diffusive clinopyroxene dissolution distance

The effective binary diffusivities and interface-melt composition can be used to calculate diffusive clinopyroxene dissolution distance (Eq. (2c)). This calculation is independent of the direct measurements shown in Table 2, and provides cross-check on the quality of the experiments. However, Eq. (2c) needs to be modified to accommodate the complexity that two components (rather than a single component) control the saturation of clinopyroxene in the melt. The modification is as follows:

$$L = 2\alpha_{\text{MgO}} \frac{\rho_m}{\rho_c} \sqrt{D_{\text{MgO}} t}, \quad (5a)$$

$$L = 2\alpha_{\text{CaO}} \frac{\rho_m}{\rho_c} \sqrt{D_{\text{CaO}} t}, \quad (5b)$$

where  $\alpha_{\text{MgO}}$  and  $\alpha_{\text{CaO}}$  satisfies:

$$\exp(\alpha_{\text{MgO}}^2) \text{erfc}(-\alpha_{\text{MgO}}) \sqrt{\pi} \alpha_{\text{MgO}} = \frac{C_0^{\text{MgO}} - C_\infty^{\text{MgO}}}{C_c^{\text{MgO}} - C_0^{\text{MgO}}}, \quad (5c)$$

$$\exp(\alpha_{\text{CaO}}^2) \text{erfc}(-\alpha_{\text{CaO}}) \sqrt{\pi} \alpha_{\text{CaO}} = \frac{C_0^{\text{CaO}} - C_\infty^{\text{CaO}}}{C_c^{\text{CaO}} - C_0^{\text{CaO}}}, \quad (5d)$$

The five unknowns ( $L$ ,  $C_0^{\text{MgO}}$ ,  $C_0^{\text{CaO}}$ ,  $\alpha_{\text{MgO}}$  and  $\alpha_{\text{CaO}}$ ) can be solved iteratively from the five equations (Eqs. (4), (5a), (5b), (5c), and 5d).

Clinopyroxene dissolution distance of each experiment is calculated using the above equations and listed in Table 2 as  $L_4$ . Glass density ( $\rho_m$ ) is taken as 2.77 g/cc (Tilley, 1922), and clinopyroxene density ( $\rho_c$ ) is taken as 3.278 g/cc (Thompson et al., 2005). Errors in  $L_4$  are obtained by letting  $D$  and  $C_0$  vary within their error bounds. The errors in melt and clinopyroxene densities and density variation along the melt compositional profiles are ignored. Hence, this error estimation is the lower limit. For all experiments except Exp# 7, the dissolution distances agree with each other.  $L_4$  for Exp# 7 is much larger than  $L_2$  and  $L_3$ . The cause for this disagreement is unclear. One possibility is that the rim of the clinopyroxene disc used in Exp# 7 was much thinner than the center. Using the rim as the reference position of the initial clinopyroxene–melt interface may underestimate the dissolution distance, leading to smaller  $L_2$  and  $L_3$ .

#### 4.5. Convective clinopyroxene dissolution in basaltic melt

In this section the results from diffusive crystal dissolution experiments are applied to model convective crystal dissolution in nature, where convection is driven by motion of the crystal due to the density difference between the crystal and the melt. Convective crystal dissolution rate ( $u$ ) depends on the thermodynamics and the kinetics and fluid dynamics of the system (Zhang et al., 1989; Kerr, 1995; Zhang and Xu, 2003):

$$u = \frac{\beta D}{\delta}, \quad (6a)$$

where  $\beta$  can be calculated as:

$$\beta = \frac{\rho_m(C_0 - C_\infty)}{\rho_c(C_c - C_0)}. \quad (6b)$$

The dimensionless parameter  $\beta$  is the ratio of two concentration differences between the interface melt and far-field melt ( $C_0 - C_\infty$ ) and between the crystal and interface melt ( $C_c - C_0$ ). It is related through  $C_0$  to the thermodynamic saturation condition and depends on temperature and pressure. The diffusivity ( $D$ ) characterizes the mass transport rate in the compositional boundary layer. The parameter  $\delta$  is the thickness of the compositional boundary layer and depends on dynamics such as the strength of the con-

vection. Overall,  $D/\delta$  represents the kinetics and fluid dynamics of the system. It also depends on temperature and pressure, but does not depend on the degree of saturation of the system. It depends slightly and indirectly on the crystal and melt compositions, because the compositions affect the diffusivities, densities and melt viscosity. In summary, the parameter  $\beta$  is a thermodynamic term, and  $D/\delta$  is a kinetic/dynamic term.

When two components determine the saturation condition as in the case of clinopyroxene, Eq. (6) must be modified as:

$$u = \frac{\beta_{\text{MgO}} D_{\text{MgO}}}{\delta_{\text{MgO}}}, \quad (7a)$$

$$u = \frac{\beta_{\text{CaO}} D_{\text{CaO}}}{\delta_{\text{CaO}}}, \quad (7b)$$

$$\beta_{\text{MgO}} = \frac{\rho_m (C_0^{\text{MgO}} - C_\infty^{\text{MgO}})}{\rho_c (C_c^{\text{MgO}} - C_0^{\text{MgO}})}, \quad (7c)$$

$$\beta_{\text{CaO}} = \frac{\rho_m (C_0^{\text{CaO}} - C_\infty^{\text{CaO}})}{\rho_c (C_c^{\text{CaO}} - C_0^{\text{CaO}})}. \quad (7d)$$

The five unknowns ( $u$ ,  $C_0^{\text{MgO}}$ ,  $C_0^{\text{CaO}}$ ,  $\beta_{\text{MgO}}$  and  $\beta_{\text{CaO}}$ ) can be solved from the five equations (Eqs. (4), (7a), (7b), (7c), and (7d)).

The boundary layer thickness  $\delta_{\text{MgO}}$  and  $\delta_{\text{CaO}}$  are estimated from fluid dynamic theories as follows (Zhang and Xu, 2003; Chen and Zhang, 2008):

- (1) Use the following three equations to solve for the Reynolds number (Re), crystal falling or rising velocity ( $U$ ) and drag coefficient ( $C_D$ ):

$$\text{Re} = \frac{2aU\rho_m}{\eta}, \quad (8a)$$

$$U = \sqrt{\frac{8ga|\rho_c - \rho_m|}{3\rho_m C_D}}, \quad (8b)$$

$$C_D = \frac{24}{\text{Re}} (1 + 0.15\text{Re}^{0.687}) + \frac{0.42}{1 + 42500\text{Re}^{-1.16}}, \quad (8c)$$

where  $a$  is the crystal radius and  $\eta$  is the melt viscosity. Eq. (8a) is the definition of the Reynolds number. Eq. (8b) is the general equation to calculate the falling or rising velocity of a rigid spherical particle in a fluid (e.g., Turcotte and Schubert, 1982). Eq. (8c) is from Clift et al. (1978) and has a relative error of  $\sim \pm 5\%$  for  $\text{Re} \leq 3 \times 10^5$ .

- (2) Calculate the compositional Peclet number (Pe) from the definition of Pe:

$$\text{Pe} = \frac{2aU}{D}. \quad (9)$$

- (3) Calculate the Sherwood number (Sh) as following, for  $\text{Re} \leq 10^5$  (Zhang and Xu, 2003):

$$\text{Sh} = 1 + (1 + \text{Pe})^{1/3} \left( 1 + \frac{0.096\text{Re}^{1/3}}{1 + 7\text{Re}^{-2}} \right). \quad (10)$$

- (4) Calculate the effective boundary layer thickness  $\delta$  from the definition of the Sherwood number Sh:

$$\delta = \frac{2a}{\text{Sh}}. \quad (11)$$

Table 5

An example of calculating convective clinopyroxene dissolution rate.

	MgO	CaO	References
<i>Conditions: 1523 K, 0.5 GPa, Di90, 1 mm radius</i>			
$C_c$ (wt%)	16.5	25.5	
$C_\infty$ (wt%)	7.05	10.8	
$C_0^{\text{MgO}} \times C_0^{\text{CaO}}$		102	Eq. (4)
$\rho_m$ (kg/m <sup>3</sup> )		2760	Lange and Carmichael (1987), Ochs and Lange (1999), Agee (1998), Ohtani and Maeda (2001)
$\rho_c$ (kg/m <sup>3</sup> )		3200	Thompson et al. (2005)
$\eta$ (Pa · s)		51.2	Hui and Zhang (2007)
$D$ (m <sup>2</sup> /s)	7.35E-12	2.43E-11	Eq. (3)
Re		2.03E-6	Solved iteratively from Eq. (8)
$U$ (m/s)		1.88E-5	
$C_D$		1.18E7	
Pe	5120	1550	Eq. (9)
Sh	18.2	12.6	Eq. (10)
$\delta$ (m)	1.10E-4	1.59E-4	Eq. (11)
$D/\delta$ (m/s)	6.70E-8	1.53E-7	
$C_0$ (wt%)	8.45	12.1	Solved iteratively from Eqs. (4) and (7)
$\beta$	0.155	0.0684	
$u$ (m/s)		1.05E-8	

Because  $\delta$  depends on Pe and hence on  $D$  (Eq. (9)),  $\delta_{\text{MgO}} \neq \delta_{\text{CaO}}$ .

An example of calculation is shown in Table 5 to demonstrate how the experimental results of this study can be plugged in the above calculation scheme. At 1523 K and 0.5 GPa, the convective dissolution rate is  $1.05 \times 10^{-8}$  m/s. If the radius of the clinopyroxene crystal is 1 mm, it would take about 1.1 days for the clinopyroxene crystal to completely dissolve. Under the same conditions, an olivine crystal would survive for about 2.4 days (Chen and Zhang, 2008). Fig. 10 shows a comparison between convective olivine and clinopyroxene dissolution, where the olivine and clinopyroxene are separated grains. The liquidus  $T$  of the basalt is  $\sim 1463$  K at 0.2 GPa. Both olivine and clinopyroxene are close to saturation at this condition. As the degree of superheating increases, dissolution rate of clinopyroxene increases more rapidly than olivine. This difference is due to the difference in the  $\beta$  terms of the two minerals.

Based on our experimental result,  $(D/\delta)_{\text{MgO}}$  and  $(D/\delta)_{\text{CaO}}$  are calculated for 1423–1723 K, 0.0001 to 2 GPa and clinopyroxene composition from Di80 to Di100 within diopside-hedenbergite binary system. The values of  $\delta_{\text{MgO}}$  and  $\delta_{\text{CaO}}$  depend only weakly on grain radius. When the radius changes from 1 to 100 mm,  $\delta_{\text{MgO}}$  and  $\delta_{\text{CaO}}$  vary by  $\sim 10\%$ . This variation is small compared to other uncertainties, thus is ignored in developing Eqs. (12a) and (12b) below.  $D/\delta$  depends strongly on temperature but only weakly on pressure within the low pressure range discussed in this study. The calculation results are fitted to the following equations:

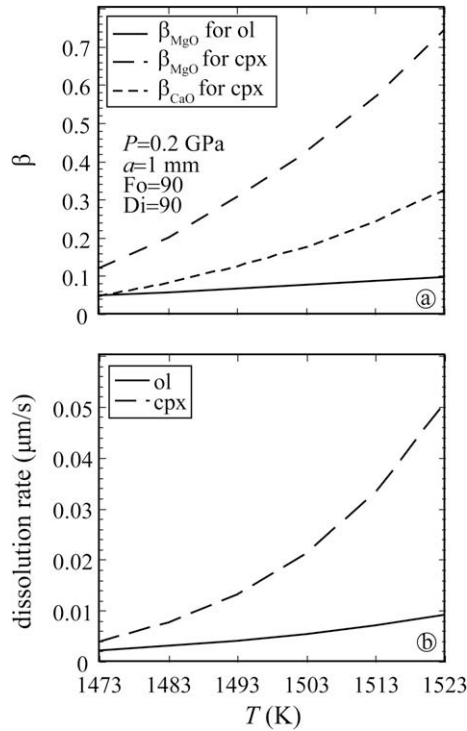


Fig. 10. Calculated  $\beta$  parameter and convective crystal dissolution rate of olivine and clinopyroxene in basalt. The clinopyroxene dissolution rate depends more strongly on  $T$  than that of olivine. This stronger dependence is largely due to the difference in the  $\beta$  parameter of the two minerals, which in turn depends on their composition and saturation status.

$$\ln\left(\frac{D}{\delta}\right)_{\text{MgO}} = 6.64(\pm 0.01) - \frac{34800(\pm 14)}{T} - 0.0760(\pm 0.0008)P - 0.299(\pm 0.008)X_{\text{Di}}, \quad (12a)$$

and

$$\ln\left(\frac{D}{\delta}\right)_{\text{CaO}} = 3.87(\pm 0.01) - \frac{29340(\pm 18)}{T} - 0.0741(\pm 0.001)P - 0.292(\pm 0.010)X_{\text{Di}}, \quad (12b)$$

where  $(D/\delta)_{\text{MgO}}$  and  $(D/\delta)_{\text{CaO}}$  are in m/s,  $T$  in K,  $P$  in GPa, and  $X_{\text{Di}}$  is the mole fraction of diopside in clinopyroxene within diopside-hedenbergite binary system (for pure diopside,  $X_{\text{Di}} = 1$ ). Eq. (12a) can reproduce the calculated  $\ln(D/\delta)_{\text{MgO}}$  values with a  $2\sigma$  error of 0.008. Eq. (12b) can reproduce the calculated  $\ln(D/\delta)_{\text{CaO}}$  values with a  $2\sigma$  error of 0.01.

Eq. (12) is based on the diffusivity in tholeiitic basalt but can be applied to alkali basalt with  $\text{SiO}_2$  content as low as 45 wt%, because the two melts have similar diffusivity and viscosity (Chen and Zhang, 2008). Extrapolating Eq. (12) to other silicate melt such as andesite may introduce errors because the diffusivity and viscosity depend on melt compositions. On the other hand, the  $\beta$  parameter can be applied to basalt and andesite ( $\text{SiO}_2$  from 47 to 56 wt%) because

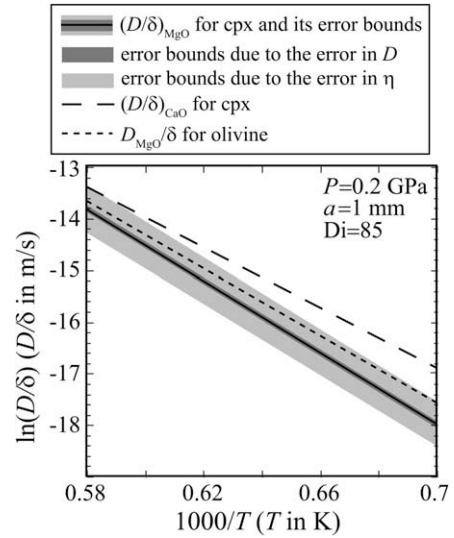


Fig. 11.  $(D/\delta)_{\text{MgO}}$  and  $(D/\delta)_{\text{CaO}}$  for clinopyroxene dissolution in basalt calculated using Eq. (12). The error bounds for  $(D/\delta)_{\text{MgO}}$  are shown. The  $(D/\delta)_{\text{MgO}}$  for olivine dissolution in basalt is calculated from Eq. (19) in Chen and Zhang (2008).

Eq. (4) is calibrated within this composition range. Section 4.7 mentions an example where this model fails, and the possible cause is that the melt composition (nephelinite with  $\sim 41$  wt%  $\text{SiO}_2$ ) is beyond the applicable range.

The uncertainty in calculating  $(D/\delta)_{\text{MgO}}$  and  $(D/\delta)_{\text{CaO}}$  mainly comes from the errors of: (1) 0.09 in  $\ln D_{\text{MgO}}$  and 0.17 in  $\ln D_{\text{CaO}}$ ; and (2) 1.4 in  $\ln \eta$  (0.61  $\log \eta$  units in Hui and Zhang, 2007) (all are  $2\sigma$  errors). The errors in melt and olivine densities and the error in the calculation scheme are much smaller than the above errors. To assess the uncertainty in  $(D/\delta)_{\text{MgO}}$  and  $(D/\delta)_{\text{CaO}}$ , we allowed  $D_{\text{MgO}}$ ,  $D_{\text{CaO}}$  and  $\eta$  to vary in their corresponding error bounds. Fig. 11 shows  $\ln(D/\delta)_{\text{MgO}}$  and  $\ln(D/\delta)_{\text{CaO}}$  as a functions of temperature. The value of  $\ln(D/\delta)_{\text{MgO}}$  varies by  $\pm 0.06$  as  $\ln(D_{\text{MgO}})$  varies within its uncertainty of  $\pm 0.09$ , and by  $\pm 0.45$  as  $\ln \eta$  varies within its uncertainty of  $\pm 1.4$ . The value of  $\ln(D/\delta)_{\text{CaO}}$  varies by  $\pm 0.12$  as  $\ln(D_{\text{MgO}})$  varies within its uncertainty of  $\pm 0.17$ , and by  $\pm 0.43$  as  $\ln \eta$  varies within its uncertainty of  $\pm 1.4$ . The error bounds for  $\ln(D/\delta)_{\text{MgO}}$  is marked by the shaded areas in Fig. 11. Assuming the errors in  $D_{\text{MgO}}$ ,  $D_{\text{CaO}}$  and  $\eta$  are not correlated, the overall uncertainty for  $\ln(D/\delta)_{\text{MgO}}$  is roughly  $\sqrt{0.06^2 + 0.45^2} \approx 0.45$  (a factor of 1.6 in  $(D/\delta)_{\text{MgO}}$ ), and that for  $\ln(D/\delta)_{\text{CaO}}$  is  $\sqrt{0.12^2 + 0.43^2} \approx 0.45$ . These values are much larger than the  $2\sigma$  errors of Eq. (12). Therefore, using Eqs. (12a) and (12b) (rather than Eqs. (3), (8a), (8b), (8c), (9), (10), and (11)) to estimate  $(D/\delta)_{\text{MgO}}$  and  $(D/\delta)_{\text{CaO}}$  would only introduce an insignificant error compared to the errors due to uncertainties in melt viscosity and diffusivities.

Fig. 11 shows that  $D_{\text{MgO}}/\delta$  for olivine dissolution in basaltic melt is only slightly greater than  $(D/\delta)_{\text{MgO}}$  for clinopyroxene dissolution and slightly smaller than  $(D/\delta)_{\text{CaO}}$ . The small difference is mainly caused by the difference in the diffusivities. When the error due to the viscosity uncertainty is considered,  $D/\delta$  for olivine and clinopyrox-

ene dissolution are within error. Further refinement of the viscosity model of natural silicate melts can significantly improve the accuracy of convective crystal dissolution models.

The error in  $\beta$  comes mainly from that in predicting  $C_0^{\text{MgO}} \times C_0^{\text{CaO}}$  (Eq. (4)). The relative error of  $\beta$  becomes unbounded as  $C_0$  approaches  $C_\infty$  (as the melt is close to clinopyroxene saturation), but the absolute error in  $\beta$  at near-saturation is about the same as that far away from saturation. Hence at near saturation, the relative error in the calculated  $u$  is large, but the absolute error does not depend on the saturation status of the system.

#### 4.6. Convective dissolution rates for olivine and clinopyroxene in a mantle xenolith in basaltic melt

The saturation of olivine is largely controlled by MgO concentration (Chen and Zhang, 2008), whereas clinopyroxene saturation is controlled by MgO and CaO. At a given  $T$  and  $P$ , an MgO–CaO plot can be used to illustrate graphically the saturation status of both olivine and clinopyroxene and the corresponding dissolution or growth rates. In the MgO–CaO plot shown as Fig. 12a, olivine saturation at a given  $T$  and  $P$  is represented by the vertical line

AB, and diopside saturation is represented by the hyperbola CD (based on Eq. (4)). To the left of AB olivine is undersaturated. And to the lower-left of CD clinopyroxene is undersaturated. Melt composition defined by point O, where AB and CD intersect, is multiply saturated with olivine and clinopyroxene. Suppose the initial melt composition is  $P_1$ , since it is to the left of AB but to the upper-right of CD, the melt is olivine undersaturated but clinopyroxene oversaturated.

Given the initial melt composition at  $T$  and  $P$ , the position of the interface melt of clinopyroxene is solely determined in the MgO–CaO diagram. Combining Eqs. (7a) and (7b) and substituting  $\beta_{\text{MgO}}$  and  $\beta_{\text{CaO}}$  from Eqs. (7c) and (7d) yields:

$$\left(\frac{D}{\delta}\right)_{\text{MgO}} \frac{C_0^{\text{MgO}} - C_\infty^{\text{MgO}}}{C_c^{\text{MgO}} - C_0^{\text{MgO}}} = \left(\frac{D}{\delta}\right)_{\text{CaO}} \frac{C_0^{\text{CaO}} - C_\infty^{\text{CaO}}}{C_c^{\text{CaO}} - C_0^{\text{CaO}}}. \quad (13)$$

Eq. (13) defines a family of linear equations of the initial melt composition ( $C_\infty^{\text{MgO}}$  and  $C_\infty^{\text{CaO}}$ ). In Fig. 12a, the two dashed lines (EF and  $P_1P_2$ ) belong to this family of equations. The significance of this family of equations is: when the initial melt composition varies along a line that satisfies Eq. (13), the interface melt composition of clinopyroxene

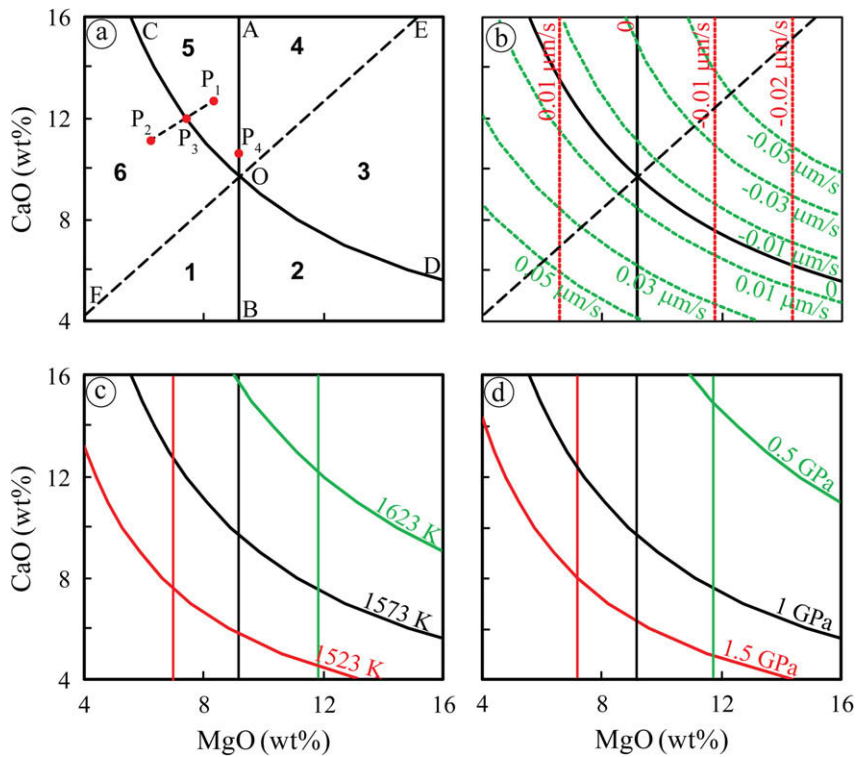


Fig. 12. MgO–CaO composition regime illustrating the saturation status of olivine and clinopyroxene. (a) Line AB represents the melt composition at olivine saturation (Eq. (17) in Chen and Zhang, 2008). To the left of AB olivine is undersaturated. Curve CD represents the melt composition at clinopyroxene saturation (Eq. (4) in this study). To the lower-left of CD clinopyroxene is undersaturated. Point O represents the melt composition that is multiply-saturated with olivine and clinopyroxene. Line EF and  $P_1P_2$  satisfy Eq. (13). During clinopyroxene dissolution, the melts with compositions falling on EF would share the fixed interface melt composition at O. Similarly, the melts with compositions falling on  $P_1P_2$  would share the fixed interface melt composition at  $P_3$ . AB, CD and EF divide the MgO–CaO diagram into six regions, numbered 1–6 in the figure. The saturation status of olivine and clinopyroxene in each of the six regions is summarized in Table 6. (b) Contour lines for convective dissolution and growth rate calculated at 1 GPa and 1573 K. The red lines are for olivine, and green ones for clinopyroxene. (c) The dependence of the saturation curves on  $T$  at 1 GPa. (d) The dependence on  $P$  at 1573 K.

Table 6  
Behavior of olivine and clinopyroxene when coexisting in xenoliths.

Initial melt composition region	Relation between the interface melt composition and the initial melt composition	Ol	Cpx	Ol growth at the cpx interface?	Surface MgO diffusion flux	
1	$C_{\infty}^{\text{MgO}} < C_{0,\text{ol}}^{\text{MgO}} < C_{0,\text{cpx}}^{\text{MgO}}$	$C_{\infty}^{\text{CaO}} < C_{0,\text{cpx}}^{\text{CaO}}$	Dissolution	Dissolution	Yes	cpx → ol
BO	$C_{\infty}^{\text{MgO}} = C_{0,\text{ol}}^{\text{MgO}} < C_{0,\text{cpx}}^{\text{MgO}}$	$C_{\infty}^{\text{CaO}} < C_{0,\text{cpx}}^{\text{CaO}}$	At saturation	Dissolution	Yes	cpx → ol
2	$C_{0,\text{ol}}^{\text{MgO}} < C_{\infty}^{\text{MgO}} < C_{0,\text{cpx}}^{\text{MgO}}$	$C_{\infty}^{\text{CaO}} < C_{0,\text{cpx}}^{\text{CaO}}$	Growth	Dissolution	Yes	cpx → ol
DO	$C_{0,\text{ol}}^{\text{MgO}} < C_{\infty}^{\text{MgO}} = C_{0,\text{cpx}}^{\text{MgO}}$	$C_{\infty}^{\text{CaO}} = C_{0,\text{cpx}}^{\text{CaO}}$	Growth	At saturation	Yes	cpx → ol
3	$C_{0,\text{ol}}^{\text{MgO}} < C_{0,\text{cpx}}^{\text{MgO}} < C_{\infty}^{\text{MgO}}$	$C_{\infty}^{\text{CaO}} < C_{0,\text{cpx}}^{\text{CaO}}$	Growth	Growth	Yes	cpx → ol
EO	$C_{0,\text{ol}}^{\text{MgO}} = C_{0,\text{cpx}}^{\text{MgO}} < C_{\infty}^{\text{MgO}}$	$C_{0,\text{cpx}}^{\text{CaO}} < C_{\infty}^{\text{CaO}}$	Growth	Growth	At saturation	No flux
4	$C_{0,\text{cpx}}^{\text{MgO}} < C_{0,\text{ol}}^{\text{MgO}} < C_{\infty}^{\text{MgO}}$	$C_{0,\text{cpx}}^{\text{CaO}} < C_{\infty}^{\text{CaO}}$	Growth	Growth	No	ol → cpx
AO	$C_{0,\text{cpx}}^{\text{MgO}} < C_{0,\text{ol}}^{\text{MgO}} = C_{\infty}^{\text{MgO}}$	$C_{0,\text{cpx}}^{\text{CaO}} < C_{\infty}^{\text{CaO}}$	At saturation	Growth	No	ol → cpx
5	$C_{0,\text{cpx}}^{\text{MgO}} < C_{\infty}^{\text{MgO}} < C_{0,\text{ol}}^{\text{MgO}}$	$C_{0,\text{cpx}}^{\text{CaO}} < C_{\infty}^{\text{CaO}}$	Dissolution	Growth	No	ol → cpx
CO	$C_{0,\text{cpx}}^{\text{MgO}} = C_{\infty}^{\text{MgO}} < C_{0,\text{ol}}^{\text{MgO}}$	$C_{0,\text{cpx}}^{\text{CaO}} = C_{\infty}^{\text{CaO}}$	Dissolution	At saturation	No	ol → cpx
6	$C_{\infty}^{\text{MgO}} < C_{0,\text{cpx}}^{\text{MgO}} < C_{0,\text{ol}}^{\text{MgO}}$	$C_{\infty}^{\text{CaO}} < C_{0,\text{cpx}}^{\text{CaO}}$	Dissolution	Dissolution	No	ol → cpx
FO	$C_{\infty}^{\text{MgO}} < C_{0,\text{cpx}}^{\text{MgO}} = C_{0,\text{ol}}^{\text{MgO}}$	$C_{\infty}^{\text{CaO}} < C_{0,\text{cpx}}^{\text{CaO}}$	Dissolution	Dissolution	At saturation	No flux

dissolution is fixed at the intersection between this line and the curve CD. For example, if the initial melt composition lies anywhere on the line  $P_1P_2$ , the interface melt composition would be fixed at  $P_3$ . A particular line in this equation family intersects AB and CD at O (line EF in Fig. 12a). Melts with initial compositions falling on EF share the common interface melt (point O) that is multiply-saturated with olivine and clinopyroxene. AB, CD and EF divide the MgO–CaO diagram into six regions, numbered 1–6 in Fig. 12a. The saturation status of olivine and clinopyroxene in each of the six regions is summarized in Table 6.

Given the initial melt composition, the position of the interface melt of olivine is not solely determined in the MgO–CaO diagram, because CaO is not buffered by olivine dissolution. The interface CaO concentration during olivine dissolution is less than that in the initial melt, and is greater than that estimated from simple dilution by olivine dissolution because of multicomponent diffusion effect (Zhang et al., 1989; Chen and Zhang, 2008).

Considering olivine and clinopyroxene, the saturation status of one mineral in the interface melt of the other may not be the same as its saturation status in the initial melt. For example, suppose the initial melt composition is at  $P_2$ , and the interface melt of olivine is at  $P_4$ . Clinopyroxene is undersaturated in the initial melt, while oversaturated in the interface melt of olivine. Hence, clinopyroxene would grow in the interface melt of olivine. Crystal growth in the interface melt will affect the crystal dissolution rate. Also note that the scenarios of the initial melt composition at  $P_1$  and  $P_2$  are different. In the former scenario, clinopyroxene could grow everywhere in the melt. In the latter scenario, clinopyroxene could only grow in the interface melt region of olivine.

Convective dissolution and growth rates of olivine and clinopyroxene at given  $T$  and  $P$  can be illustrated in the MgO–CaO diagram. Fig. 12b shows the contoured lines for the dissolution and growth rates at 1 GPa and

1573 K. The olivine composition is assumed to be Fo90, and clinopyroxene Di90 (within diopside-hedenbergite binary system). Dissolution rates are positive numbers, and growth rates are negative numbers. The effects caused by possible crystal growth in the interface melt and some complicating factors for crystal growth (such as nucleation and dendritic growth) are not considered in the calculation. The contour lines can be viewed as expressions for the  $\beta$  parameters, because the  $P$ ,  $T$  and mineral compositions are fixed, hence the  $D/\delta$  parameters are constants. The contour lines of clinopyroxene dissolution rate are denser than those of olivine, meaning the  $\beta$  parameter of clinopyroxene depends more strongly on the melt composition than that of olivine.

Since olivine and clinopyroxene co-exist in mantle xenoliths, the difference in the interface melt compositions would lead to diffusion along the xenoliths surface, in addition to the diffusion between the xenoliths surface and far-field melt. This additional diffusion will affect the dissolution rate. For example, suppose the initial melt composition is at  $P_2$ , the interface melt of clinopyroxene is at  $P_3$ , and the interface melt of olivine is at  $P_4$  (Fig. 12a).  $P_3$  has lower MgO and higher CaO than  $P_4$ . Hence MgO would diffuse from the olivine surface toward the clinopyroxene surface, and CaO diffuses the opposite direction. Not considering the growth of clinopyroxene in the interface melt of olivine, olivine dissolution would be enhanced, because its overall MgO diffusion flux is enhanced. The change in the dissolution rate of clinopyroxene is uncertain, because the MgO and CaO fluxes are affected in opposite directions. When the initial melt composition falls on EF, the diffusion flux becomes zero.

The positions of lines AB, CD and EF depend on  $P$  and  $T$ . Fig. 12c shows the temperature dependence at 1 GPa. Fig. 12d shows the pressure dependence at 1573 K. The dependence can be utilized to infer the thermal history of the system from the interaction between the xenoliths and host basalt.

#### 4.7. Applications

Given  $T$ ,  $P$  and the initial melt composition, the behavior of xenoliths can be predicted. For example, [Morgan and Liang \(2005\)](#) conducted lherzolite reactive dissolution experiments in an alkali basalt (47.10 wt% SiO<sub>2</sub>) and a basaltic andesite (54.86 wt% SiO<sub>2</sub>) at 1 GPa and 1573 K. They observed dissolution of olivine and clinopyroxene and precipitation of orthopyroxene in the basaltic andesite, and dissolution of clinopyroxene and orthopyroxene and precipitation of olivine in the alkali basalt. [Fig. 13](#) shows the behavior of olivine and clinopyroxene in these melts predicted by our saturation models. The details about constructing such an MgO–CaO diagram are listed in [Table 7](#). Our model is consistent with the dissolution of olivine and clinopyroxene in the basaltic andesite. For the alkali basalt, the experimental data fall within error (the shaded areas) of the saturation curves, and the reaction of olivine and clinopyroxene cannot be unambiguously determined. Note that the model calculations should not be extrapolated too much outside the calibrated melt composition range, with SiO<sub>2</sub> from 47 wt% to 56 wt% (see caption of [Fig. 1](#)). A trial calculation for a nephelinite melt containing 41 wt% SiO<sub>2</sub> did not match experimental results.

Another application is to infer the  $T$ – $P$  conditions from reactions between mantle minerals and melt. For example, [Stolper et al. \(2004\)](#) proposed that melt with 48–50 wt% SiO<sub>2</sub> (named high-Si and high-(Ca, Al) melts) found in the Hawaii Scientific Drilling Project might originate from more primitive melts with 46–48 wt% SiO<sub>2</sub> (named low-Si melt). The low-Si melt was inferred to be formed by partial melting of a lherzolithic mantle at 3–4 GPa. During its ascending, it crystallized olivine and dissolved orthopyroxene and clinopyroxene of the overlying mantle, which changed its composition to be the high-Si and high-(Ca, Al) melts. As shown in [Fig. 14](#), at plausible pressure range of 1.5–2 GPa, to have the high-Si and high-(Ca, Al) melts close to olivine saturation while keep the low-Si melt to

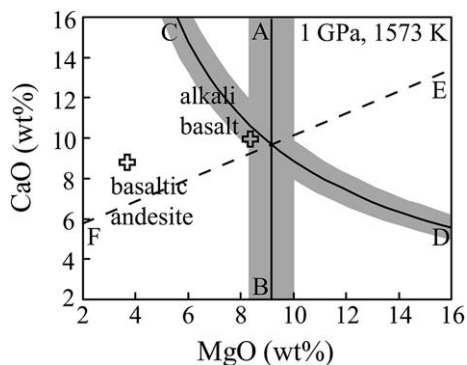


[Fig. 13](#). Test of the olivine and clinopyroxene saturation models using experimental results of [Morgan and Liang \(2005\)](#). Line AB represents the melt composition at olivine saturation, and curve CD represents the melt composition at clinopyroxene saturation. The shaded areas represent the model errors. [Morgan and Liang \(2005\)](#) observed dissolution of olivine and clinopyroxene in the basaltic andesite, and dissolution of clinopyroxene and precipitation of olivine in the alkali basalt. The details on constructing this figure are listed in [Table 7](#).

[Table 7](#)  
Details of constructing [Fig. 13](#).

Parameter	Reference
$T = 1573$ K	
$P = 1$ GPa	
The clinopyroxene composition:	<a href="#">Morgan and Liang (2005)</a>
$C_{\text{cpx}}^{\text{MgO}} = 17.54$ wt%	
$C_{\text{cpx}}^{\text{CaO}} = 18.98$ wt%	
$X_{\text{Di}} = 0.91$	
Line AB: the interface melt of olivine	$\ln C = 7.82 + 2.66 P - \frac{8040}{T} - \frac{4960P}{T}$ , Eq. (17) in <a href="#">Chen and Zhang (2008)</a>
$C_0^{\text{MgO}} = 9.17 \pm 0.86$ wt%	
Curve CD: the interface melt of clinopyroxene ( $C$ in wt%):	
$C_0^{\text{MgO}} \times C_0^{\text{CaO}} = 88.83_{-9.36}^{+10.46}$	Eq. (4)
Point O: the composition of a melt that is multiply saturated with olivine and clinopyroxene:	
$C_0^{\text{MgO}} = 9.17$ wt%	
$C_0^{\text{CaO}} = 9.69$ wt%	
$\left(\frac{D}{\delta_{\text{MgO}}}\right) = 1.33 \times 10^{-7}$ m/s	Eq. (12a)
$\left(\frac{D}{\delta_{\text{CaO}}}\right) = 2.71 \times 10^{-7}$ m/s	Eq. (12b)
Line EF:	
$1.33 \times 10^{-7} \frac{9.17 - C_{\infty}^{\text{MgO}}}{17.54 - 9.17} = 2.17$	Eq. (13)
$\times 10^{-7} \frac{9.69 - C_{\infty}^{\text{CaO}}}{18.98 - 9.69}$	

be clinopyroxene under-saturated and olivine over-saturated, the temperature range is 1713–1738 K. Considering the model errors (shaded zones in [Fig. 14](#)), the possible temperature range is 1673–1743 K. These values are in rough agreement with the partial melting temperatures of 1770–1849 K estimated by [Putirka \(2008; his Table DR1\)](#).

[Lissenberg and Dick \(2008\)](#) studied the texture and chemical composition of the gabbro at the Kane Megamullion, mid-Atlantic ridge. They proposed that the high-Mg# clinopyroxene in the gabbro is formed by the reaction between mid-ocean ridge basalt and primitive cumulates in the lower oceanic crust, instead of high pressure crystallization. In the context of their model, olivine and plagioclase dissolved into the basaltic melt, and clinopyroxene and new plagioclase with lower anorthite content precipitated. We calculate whether it is possible for the two model basaltic melts in [Lissenberg and Dick \(2008\)](#) to be olivine undersaturated and clinopyroxene oversaturated at the pressure of 0.15 GPa. [Fig. 15a](#) shows that at about 1438 K and 0.15 GPa, the two model basaltic melts are olivine undersaturated and clinopyroxene oversaturated. As temperature increases, the two melts become undersaturated with respect to both olivine and clinopyroxene ([Fig. 15b](#)). Hence, our calculation shows that the mechanism proposed by [Lissenberg and Dick \(2008\)](#) is possible. Furthermore, the temperature for such reactions is inferred to be about 1438 K. Considering model uncertainties, the

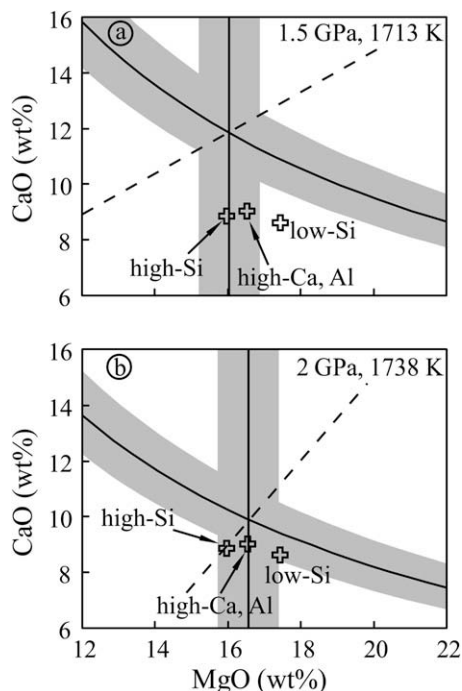


Fig. 14. Application of the olivine and clinopyroxene saturation models to the petrogenesis model on Hawaii basalts (indicated by crosses). Stolper *et al.* (2004) proposed that the melts with 46–48 wt% SiO<sub>2</sub> (low-Si melt) crystallized olivine and dissolved orthopyroxene and clinopyroxene during its ascending, producing the melt with 48–50 wt% SiO<sub>2</sub> (high-Si and high-(Ca, Al) melts). The *T* is around 1713–1738 K at 1.5–2 GPa to satisfy the olivine saturation in the high-Si and high-(Ca, Al) melts, and the clinopyroxene under-saturation in the low-Si melt.

possible temperature range for such reactions is 1393–1493 K.

The last example is from a basalt from Kuandian, Northeast China, which contains abundant mantle xenolith, mainly spinel lherzolite. The basalt contains 48.72 wt% SiO<sub>2</sub>, 7.92 wt% MgO and 7.51 wt% CaO (KD-HY-3a in Chen *et al.*, 2007). It has a porphyritic texture, with about 5% olivine phenocrysts. The olivine phenocrysts are up to 300 μm in diameter. The groundmass consists of clinopyroxene, plagioclase and Fe-Ti oxides, which are about 10–30 μm. Fig. 16 shows a contact between the host basalt and a xenolith. The olivine in the xenoliths has a homogeneous core and an Fe-rich rim. No embayment can be observed along the edge of the core. The composition of the rim changes gradually, with the inner part being Mg-rich and the outer part being Fe-rich. No distinct boundary can be observed between the core and the rim. These features could be due to olivine growth or diffusion in the olivine (e.g., Klügel, 1998; Liang, 2000; Shaw and Klügel, 2002). The basalt is inferred to be olivine oversaturated. The basalt could not be olivine under-saturated because dissolution texture is not observed and because of the relatively large olivine phenocrysts. The clinopyroxene also has a homogeneous core and an Fe-rich rim. The boundary between the core and the rim, however, is quite distinct. Embayment is frequently seen along the boundary.

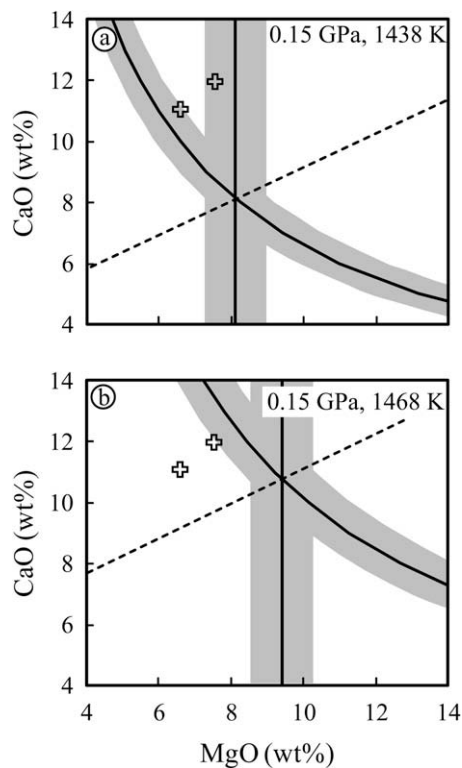


Fig. 15. Application of the olivine and clinopyroxene saturation models to the petrogenesis model on mid-ocean ridge basalts (indicated by crosses). Lissenberg and Dick (2008) proposed that olivine and plagioclase dissolved in the basalt, while clinopyroxene and new plagioclase precipitated. Constrained by olivine under-saturation and clinopyroxene over-saturation, the *T* is around 1438 K.

The rim contains pockets of glass and regions that have similar composition as the core. These features suggest that clinopyroxene was first dissolved after entrainment and then some crystals grew. The boundary between the core and the rim may hence be interpreted as the dissolution front. The non-straight dissolution front may be attributed to the cleavages in the clinopyroxene, as observed in our experiments.

Besides olivine oversaturation and clinopyroxene under-saturation, another constraint is the dissolution distance of clinopyroxene. Based on the preservation of the shape of the olivine and clinopyroxene in Fig. 16a, the dissolution distance of clinopyroxene is inferred to be small, likely no more than 100 μm. Assuming a plausible ascent rate range of 0.1–10 m/s (Demouchy *et al.*, 2006; Peslier and Luhr, 2006), if the dissolution started at 2 GPa and ended after eruption, the average dissolution rate should be no more than 0.015 μm/s. If the dissolution started at 1 GPa and ended after eruption, the average dissolution rate should be no more than 0.03 μm/s.

To satisfy the olivine oversaturation and clinopyroxene undersaturation constraints at 1 GPa (Fig. 17a), the temperature could be about 1538 K. Considering the model errors (shaded zones in Fig. 17), the possible temperature range is 1523–1563 K. The maximum dissolution rate is 0.016 μm/s, satisfying the dissolution rate constraint of less

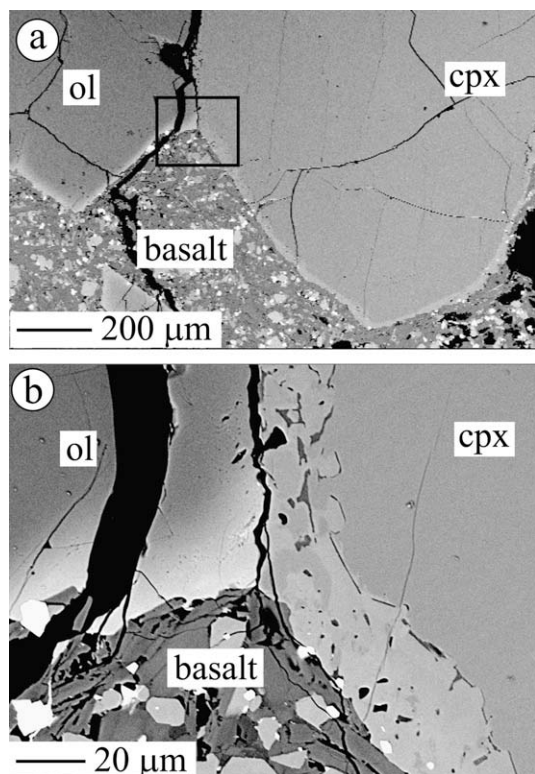


Fig. 16. BSE images showing olivine and clinopyroxene reactive textures between a mantle xenolith and its host basalt from Kuandian, Northeast China. (a) An overall view; (b) a zoomed-in view of the box area in (a). The contrasting textures of olivine and clinopyroxene suggest olivine over-saturation and clinopyroxene under-saturation in the host basalt.

than  $0.03 \mu\text{m/s}$ . At 2 GPa, to satisfy the clinopyroxene undersaturation and the dissolution rate constraints (Fig. 17b), the temperature could be 1613 K. Considering the model errors, the possible temperature range is 1588–1628 K, which also satisfies the olivine oversaturation constraint. Overall, the possible temperature range for the basalt at 1.5–2 GPa is 1523–1628 K.

In the above examples the errors in the estimated reaction temperatures mainly come from the errors in the saturation models and the uncertainty in the entrainment pressure. Further constraint on the plausible pressure range can help to refine the estimations.

## 5. CONCLUSIONS

The effective binary diffusivities of MgO and CaO,  $D_{\text{MgO}}$  and  $D_{\text{CaO}}$ , and the concentrations of MgO and CaO in the interface melt,  $C_0^{\text{MgO}}$  and  $C_0^{\text{CaO}}$ , are extracted from diffusion-controlled clinopyroxene dissolution experiments.  $D_{\text{MgO}}$  and  $D_{\text{CaO}}$  show Arrhenian dependence on temperature. The pressure dependence is small and not resolved within 0.47–1.90 GPa. Clinopyroxene saturation is treated as being determined by  $C_0^{\text{MgO}} \times C_0^{\text{CaO}}$ . The saturation condition is modeled as a function of temperature and pressure.

For convenient calculation of convective dissolution rates,  $(D/\delta)_{\text{MgO}}$  and  $(D/\delta)_{\text{CaO}}$  values (where  $\delta$  is the

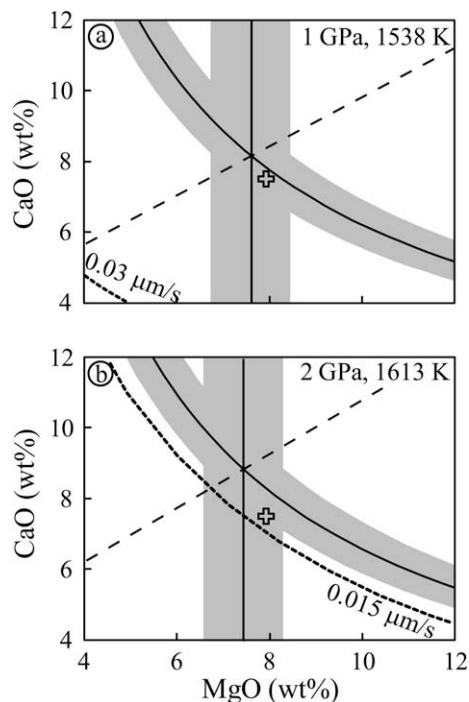


Fig. 17. Application of the olivine and clinopyroxene saturation models to the basalt from Kuandian, Northeast China. In addition to the olivine saturation and clinopyroxene under-saturation constraints, the dissolution rate is inferred to be no more than  $0.03 \mu\text{m/s}$  if the entrainment pressure was 1 GPa, and no more than  $0.015 \mu\text{m/s}$  if the entrainment pressure was 2 GPa, represented by the dashed curves.

boundary layer melt thickness next to a falling clinopyroxene crystal) for Di80–100 clinopyroxene are calculated within 1423–1723 K and 0.0001–2 GPa, and are given as functions of  $T$ ,  $P$ , and  $X_{\text{Di}}$ . The uncertainty in both  $(D/\delta)_{\text{MgO}}$  and  $(D/\delta)_{\text{CaO}}$  is a factor of  $\sim 1.6$ , mainly due to the uncertainties in viscosity. The kinetics and fluid dynamics of convective clinopyroxene dissolution in basalt, characterized by the  $(D/\delta)_{\text{MgO}}$  and  $(D/\delta)_{\text{CaO}}$  values, are similar to that of convective olivine dissolution in basalt (Chen and Zhang, 2008). Clinopyroxene dissolution rate depends more strongly on the degree of superheating and the composition of the melt than that of olivine. This difference is mainly due to the difference in the  $\beta$  terms of the two minerals.

The crystal dissolution models in this study and Chen and Zhang (2008) are applied to melt-mineral reactions at Hawaii (Stolper et al., 2004), mid-Atlantic ridge (Lissenberg and Dick, 2008) and Kuandian, Northeast China (Chen et al., 2007). The temperature for the proposed olivine crystallization and clinopyroxene dissolution in Hawaii basalts is inferred to be 1673–1743 K at 1.5–2 GPa. The temperature of the proposed olivine dissolution and clinopyroxene precipitation in mid-ocean ridge basalt is inferred to be 1393–1493 K at lower oceanic crust pressure of 0.15 GPa. For Kuandian basalts, the temperature is inferred to be 1523–1628 K at 1–2 GPa.

## ACKNOWLEDGMENTS

We appreciate the critical and constructive reviews of J.K. Russell, K. Putirka, C.S.J. Shaw and an anonymous reviewer. Y. Chen thanks Zhengjiu Xu, Hejiu Hui and Huaiwei Ni, for training and help on piston-cylinder experiments and FTIR measurement. This work is supported by NSF Grants EAR-0537598, 0711050 and 0838127. Electron microprobe work is carried out on a Cameca SX100 instrument at Electron Microbeam Analysis Laboratory of the University of Michigan, which is supported by NSF Grant 9911352.

## APPENDIX A. SUPPLEMENTARY DATA

Supplementary data associated with this article can be found, in the online version, at [doi:10.1016/j.gca.2009.06.016](https://doi.org/10.1016/j.gca.2009.06.016).

## REFERENCES

- Agee C. B. (1998) Crystal–liquid density inversions in terrestrial and lunar magmas. *Phys. Earth Planet. Interiors* **107**, 63–74.
- Asimow P. D. and Ghiorso M. S. (1998) Algorithmic modifications extending MELTS to calculate subsolidus phase relations. *Am. Mineral.* **83**, 1127–1131.
- Baker D. R. (1990) Chemical interdiffusion of dacite and rhyolite: anhydrous measurements at 1 atm and 10 kbar, application of transition state theory, and diffusion in zoned magma chambers. *Contrib. Mineral. Petrol.* **104**, 407–423.
- Bell D. R. and Rossman G. R. (1992) Water in Earth's mantle – the role of nominally anhydrous minerals. *Science* **255**, 1391–1397.
- Boyd F. R. and England J. L. (1963) Effect of pressure on the melting of diopside,  $\text{CaMgSi}_2\text{O}_6$ , and albite,  $\text{NaAlSi}_3\text{O}_8$ , in the range up to 50 kilobars. *J. Geophys. Res.* **68**, 311–323.
- Brearley M. and Scarfe C. M. (1986) Dissolution rates of upper mantle minerals in an alkali basalt melt at high pressure: an experimental study and implications for ultramafic xenolith survival. *J. Petrol.* **27**, 1157–1182.
- Chen Y., Zhang Y., Graham D., Su S. and Deng J. (2007) Geochemistry of Cenozoic basalts and mantle xenoliths in Northeast China. *Lithos* **96**, 108–126.
- Chen Y. and Zhang Y. (2008) Olivine dissolution in basaltic melt. *Geochim. Cosmochim. Acta* **72**, 4756–4777.
- Clift R., Grace J. R. and Weber M. E. (1978) *Bubbles, Drops, and Particles*. Academic Press, New York.
- Crank J. (1975) *The Mathematics of Diffusion*. Oxford University Press, Oxford, 414 pp.
- Demouchy S., Jacobsen S. D., Gaillard F. and Stern C. R. (2006) Rapid magma ascent recorded by water diffusion profiles in olivine from Earth's mantle. *Geology* **34**, 429–432.
- Dixon J. E., Clague D. A. and Eissen J.-P. (1986) Gabbroic xenoliths and host ferrobalt from the Southern Juan de Fuca Ridge. *J. Geophys. Res.* **91**, 3795–3820.
- Dixon J. E., Stolper E. and Delaney J. R. (1988) Infrared spectroscopic measurements of  $\text{CO}_2$  and  $\text{H}_2\text{O}$  in Juan de Fuca Ridge basaltic glasses. *Earth Planet. Sci. Lett.* **90**, 87–104.
- Gavrilenko P. and Keppler H. (2007) Water solubility in clinopyroxene. *Geochimica et Cosmochimica Acta Suppl.* **S71**, A312.
- Ghiorso M. S. and Sack R. O. (1995) Chemical mass transfer in magmatic processes. IV. A revised and internally consistent thermodynamic model for the interpolation and extrapolation of liquid–solid equilibria in magmatic systems at elevated temperatures and pressures. *Contrib. Mineral. Petrol.* **119**, 197–212.
- Hui H. and Zhang Y. (2007) Toward a general viscosity equation for natural anhydrous and hydrous silicate melts. *Geochim. Cosmochim. Acta* **71**, 403–416.
- Hui H., Zhang Y., Xu Z. and Behrens H. (2008) Pressure dependence of the speciation of dissolved water in rhyolitic melts. *Geochim. Cosmochim. Acta* **72**, 3229–3240.
- Kerr R. C. (1995) Convective crystal dissolution. *Contrib. Mineral. Petrol.* **121**, 237–246.
- Klügel A. (1998) Reactions between mantle xenoliths and host magma beneath La Palma (Canary Islands): constraints on magma ascent rates and crustal reservoirs. *Contrib. Mineral. Petrol.* **131**, 237–257.
- Kress V. C. and Ghiorso M. S. (1995) Multicomponent diffusion in basaltic melts. *Geochim. Cosmochim. Acta* **59**, 313–324.
- Kubicki J. D., Muncill C. E. and Lasaga A. C. (1990) Chemical diffusion in melts on the  $\text{CaMgSi}_2\text{O}_6$ – $\text{CaAl}_2\text{Si}_2\text{O}_8$  join under high pressures. *Geochim. Cosmochim. Acta* **54**, 2709–2715.
- Kuo L.-C. and Kirkpatrick R. J. (1985) Kinetics of crystal dissolution in the system diopside–forsterite–silica. *Am. J. Sci.* **285**, 51–90.
- Lange R. A. and Carmichael I. S. E. (1987) Densities of  $\text{Na}_2\text{O}$ – $\text{K}_2\text{O}$ – $\text{CaO}$ – $\text{MgO}$ – $\text{FeO}$ – $\text{Fe}_2\text{O}_3$ – $\text{TiO}_2$ – $\text{SiO}_2$  liquids: new measurements and derived partial molar properties. *Geochim. Cosmochim. Acta* **51**, 2931–2946.
- Liang Y. (1999) Diffusive dissolution in ternary systems: analysis with applications to quartz and quartzite dissolution in molten silicates. *Geochim. Cosmochim. Acta* **63**, 3983–3995.
- Liang Y. (2000) Dissolution in molten silicates: effects of solid solution. *Geochim. Cosmochim. Acta* **64**, 1617–1627.
- Lissenberg C. J. and Dick H. J. B. (2008) Melt–rock reaction in the lower oceanic crust and its implications for the genesis of mid-ocean ridge basalt. *Earth Planet. Sci. Lett.* **271**, 311–325.
- Morgan Z. and Liang Y. (2005) An experimental study of the kinetics of lherzolite reactive dissolution with applications to melt channel formation. *Contrib. Mineral. Petrol.* **150**, 369–385.
- Morgan Z., Liang Y. and Hess P. (2006) An experimental study of anorthosite dissolution in lunar picritic magmas: implications for crustal assimilation processes. *Geochim. Cosmochim. Acta* **70**, 3477–3491.
- Ochs, III, F. A. and Lange R. A. (1999) The density of hydrous magmatic liquids. *Science* **283**, 1314–1317.
- Ohtani E. and Maeda M. (2001) Density of basaltic melt at high pressure and stability of the melt at the base of the lower mantle. *Earth Planet. Sci. Lett.* **193**, 69–75.
- Peslier A. H. and Luhr J. R. (2006) Hydrogen loss from olivines in mantle xenoliths from Simcoe (USA) and Mexico: mafic alkali magma ascent rates and water budget of the sub-continental lithosphere. *Earth Planet. Sci. Lett.* **242**, 302–319.
- Putirka K. (1999) Clinopyroxene + liquid equilibria to 100 kbar and 2450 K. *Contrib. Mineral. Petrol.* **135**, 151–163.
- Putirka K. (2008) Excess temperatures at ocean islands: implications for mantle layering and convection. *Geology* **36**, 283–286.
- Scarfe C. M., Takahashi E. and Yoder, Jr., H. S. (1980) Rates of dissolution of upper mantle minerals in an alkali-olivine basalt melt at high pressure. *Carnegie Institution Year Book* **79**, 290–296.
- Shaw C. S. J. (2000) The effect of experiment geometry on the mechanism and rate of dissolution of quartz in basanite at 0.5 GPa and 1350 °C. *Contrib. Mineral. Petrol.* **139**, 509–525.
- Shaw C. S. J. and Klügel A. (2002) The pressure and temperature conditions and timing of glass formation in mantle-derived xenoliths from Baarley, West Eifel, Germany: the case for amphibole breakdown, lava infiltration and mineral–melt reaction. *Mineral. Petrol.* **74**, 163–187.
- Shaw C. S. J. and Dingwell D. B. (2008) Experimental peridotite–melt reaction at one atmosphere: a texture and chemical study. *Contrib. Mineral. Petrol.* **155**, 199–214.

- Sparks R. S. J., Huppert H. E. and Turner J. S. (1984) The fluid dynamics of evolving magma chambers. *Phil. Trans. Roy. Soc. London*. **A310**, 500–534.
- Stolper E., Sherman S., Garcia M., Baker M. and Seaman C. (2004) Glass in the submarine section of the HSDP2 drill core, Hilo, Hawaii. *Geochem. Geophys. Geosyst.* **5**. doi:10.1029/2003GC000553.
- Thompson R. M., Downs R. T. and Redhammer G. J. (2005) Model pyroxenes III: volume of C2/c pyroxene at mantle  $P$ ,  $T$ , and  $x$ . *Am. Mineralogist* **90**, 1840–1851.
- Tilley C. E. (1922) Density, refractivity, and composition relations of some natural glasses. *Mineral. Mag.* **19**, 275–294.
- Turcotte D. L. and Schubert G. (1982) *Geodynamics: Applications of Continuum Physics to Geological Problems*. Wiley & Sons, New York, NY, p. 450.
- Van Orman J. A. and Grove T. L. (2000) Origin of lunar high-titanium ultramafic glasses: Constraints from phase relations and dissolution kinetics of clinopyroxene-ilmenite cumulates. *Meteoritics Planet. Sci.* **35**, 783–794.
- Williams D. W. and Kennedy G. C. (1969) Melting curve of diopside to 50 kilobars. *J. Geophys. Res.* **74**, 4359–4365.
- Zhang Y. (2005) Fate of rising CO<sub>2</sub> droplets in seawater. *Environ. Sci. Technol.* **39**, 7719–7724.
- Zhang Y. (2008) *Geochemical Kinetics*. Princeton University Press, Princeton, NJ.
- Zhang Y. and Behrens H. (2000) H<sub>2</sub>O diffusion in rhyolitic melts and glasses. *Chem. Geol.* **169**, 243–262.
- Zhang Y. and Xu Z. (2003) Kinetics of convective crystal dissolution and melting, with applications to methane hydrate dissolution and dissociation in seawater. *Earth Planet. Sci. Lett.* **213**, 133–148.
- Zhang Y. and Xu Z. (2008) “Fizzics” of bubble growth in beer and champagne. *Elements* **4**, 47–49.
- Zhang Y., Walker D. and Leshner C. E. (1989) Diffusive crystal dissolution. *Contrib. Mineral. Petrol.* **102**, 495–513.

Associate editor: J. Kelly Russell

## Electronic Annex 1

### Table of Contents

Compositional profiles in the glass.....	2
Fittings to the compositional profiles.....	11
Far-field melt compositions.....	21

Compositional profiles in the glass

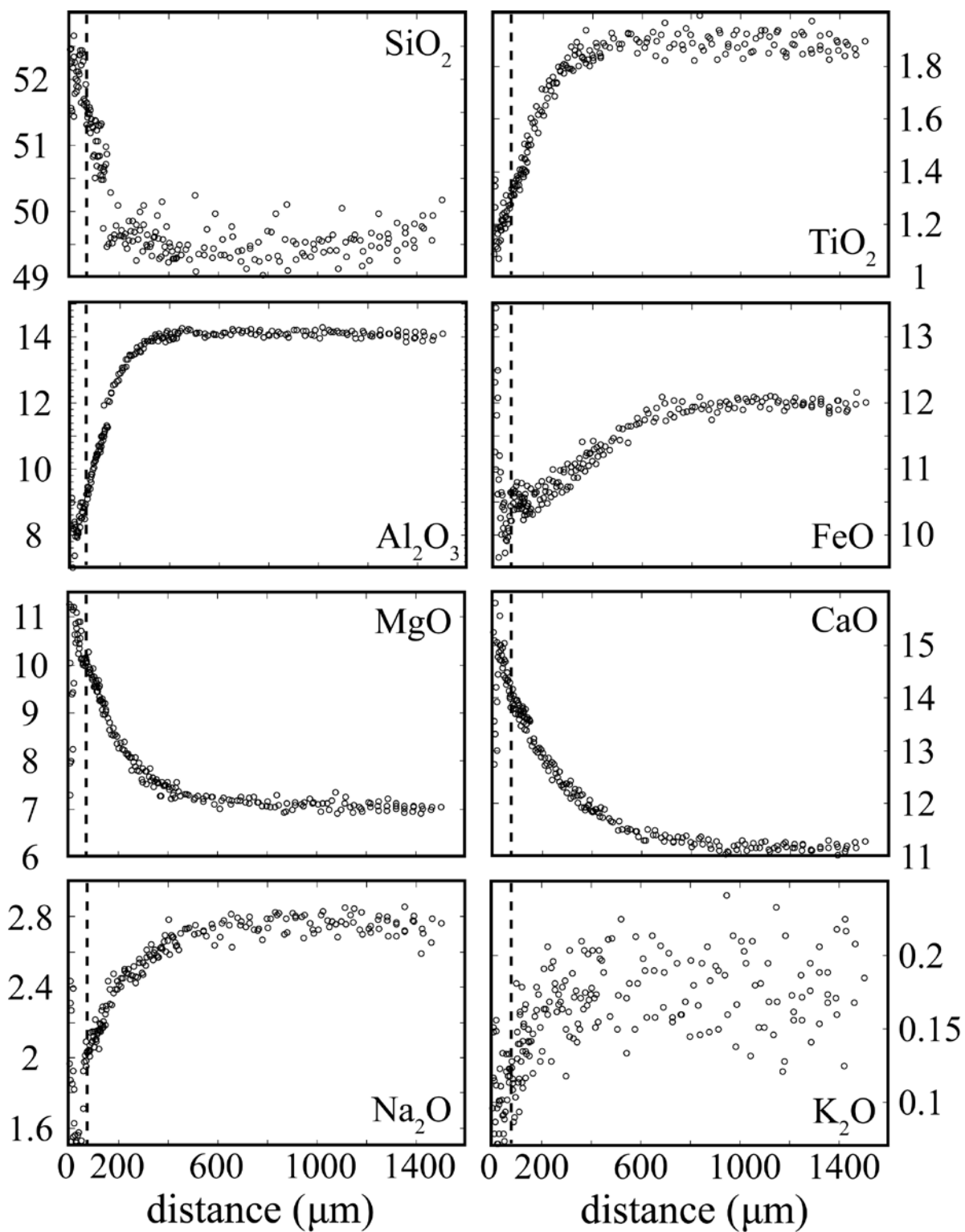


Figure A1. Compositional profiles of Exp#5 (1635 K, 0.95 GPa, 12 minutes). The vertical axes are oxide concentrations in wt%. The horizontal axis is the distance to the clinopyroxene-glass interface. Maximum extent of the quench crystals is marked by the dashed vertical lines.

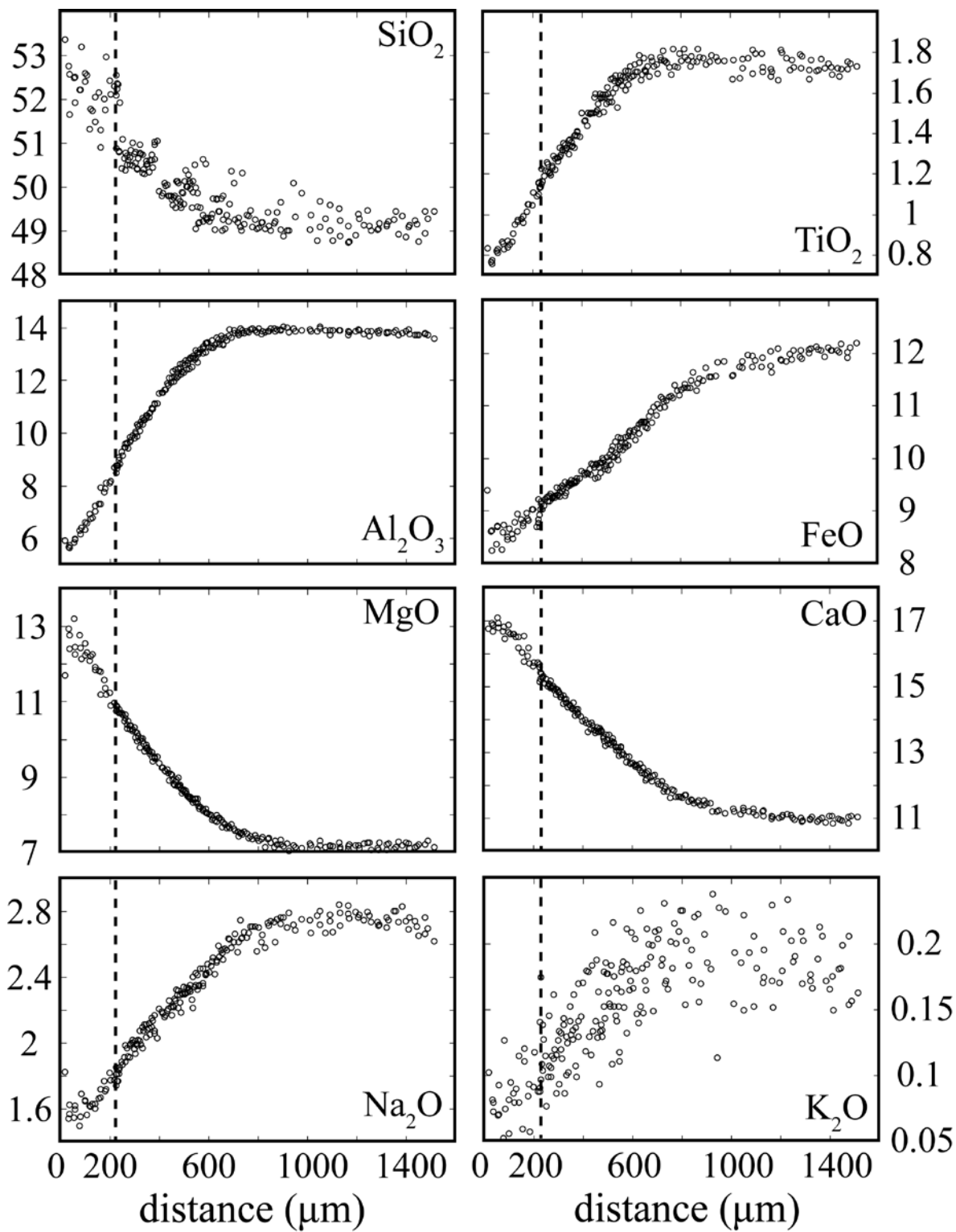


Figure A2. Compositional profiles of Exp#6 (1719 K, 1.42 GPa, 12 minutes). The vertical axes are oxide concentrations in wt%. The horizontal axis is the distance to the clinopyroxene-glass interface. Maximum extent of the quench crystals is marked by the dashed vertical lines.

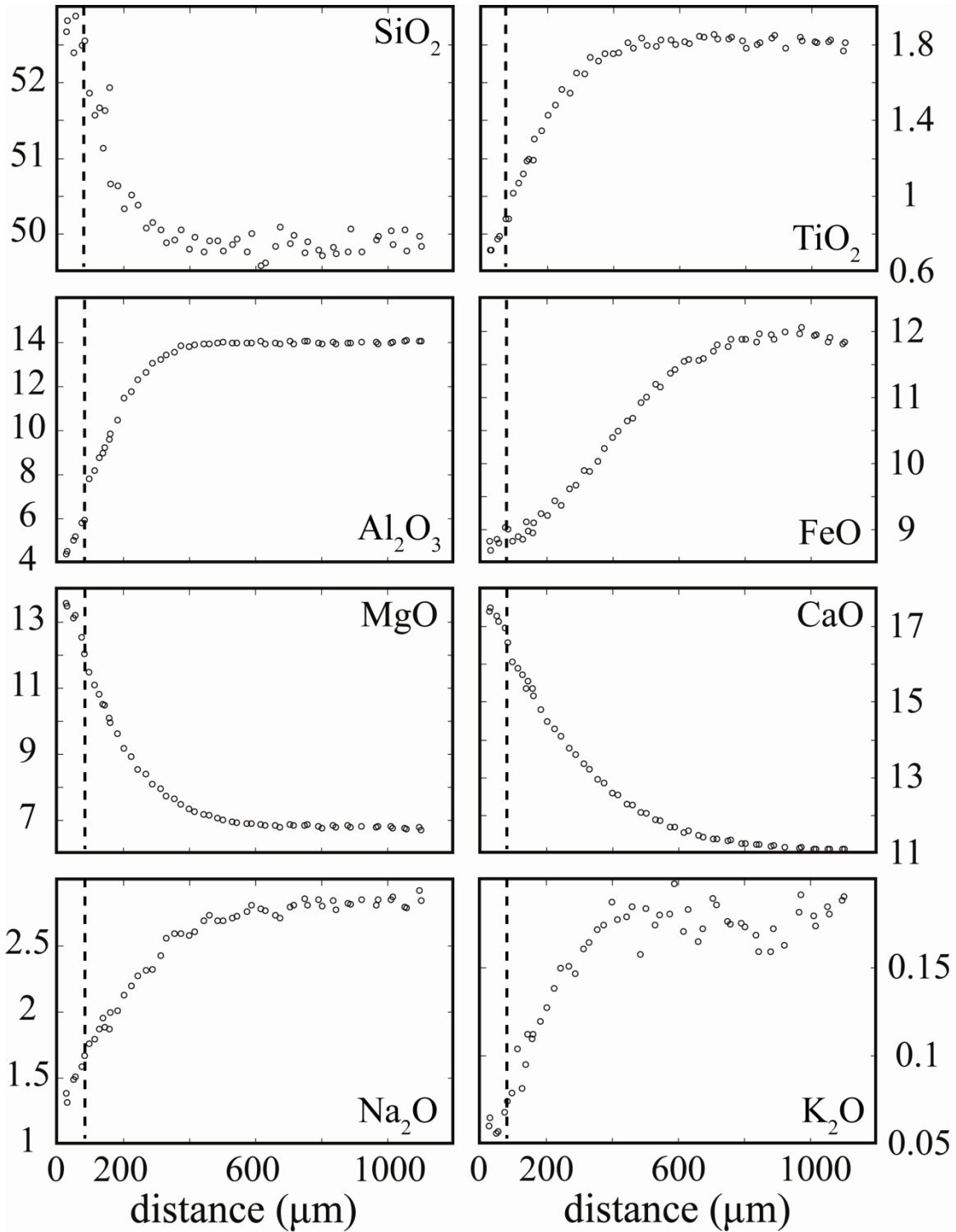


Figure A3. Compositional profiles of Exp#7 (1594 K, 0.47 GPa, 10 minutes). The vertical axes are oxide concentrations in wt%. The horizontal axis is the distance to the clinopyroxene-glass interface. Maximum extent of the quench crystals is marked by the dashed vertical lines.

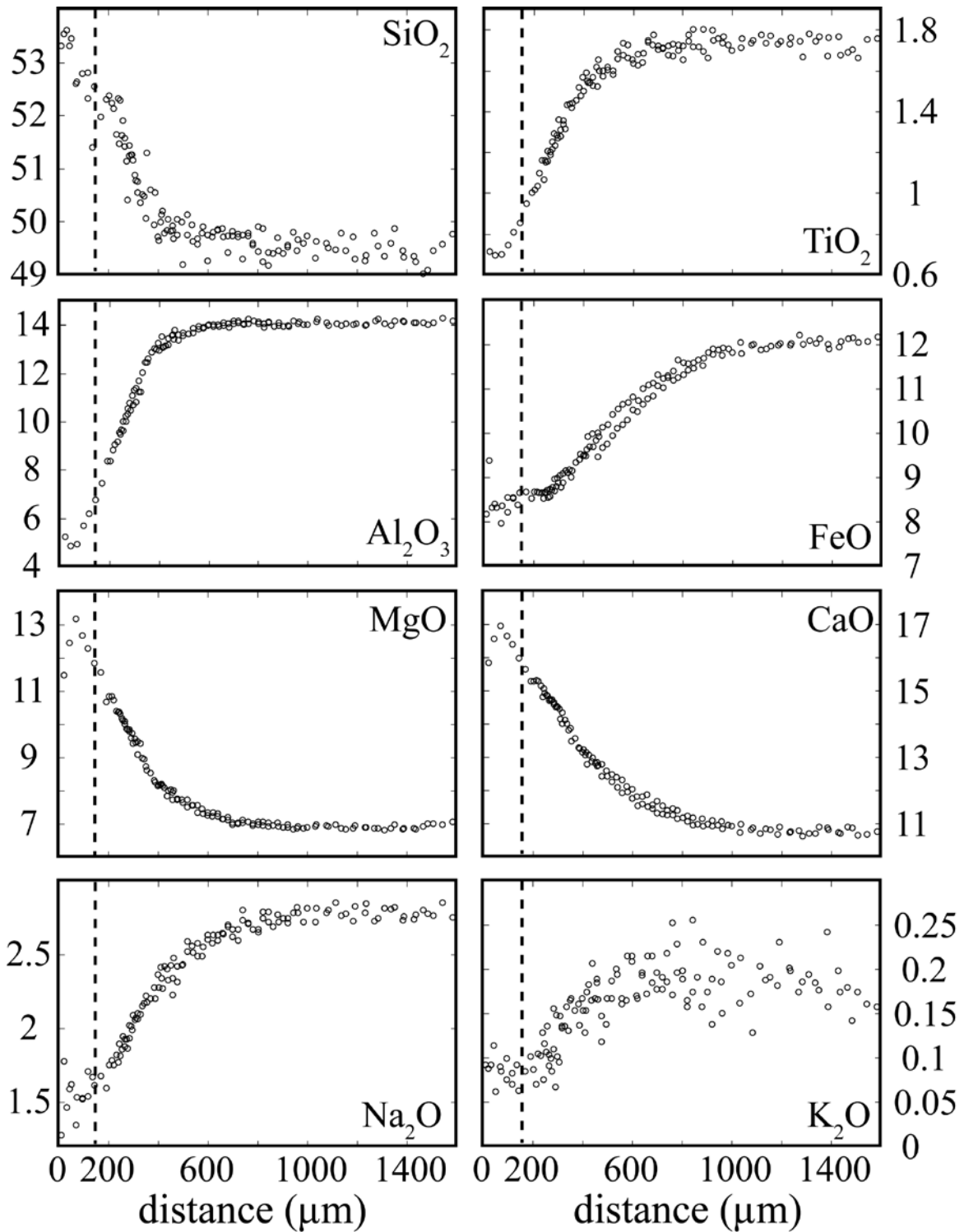


Figure A4. Compositional profiles of Exp#8 (1667 K, 0.95 GPa, 12 minutes). The vertical axes are oxide concentrations in wt%. The horizontal axis is the distance to the clinopyroxene-glass interface. Maximum extent of the quench crystals is marked by the dashed vertical lines.

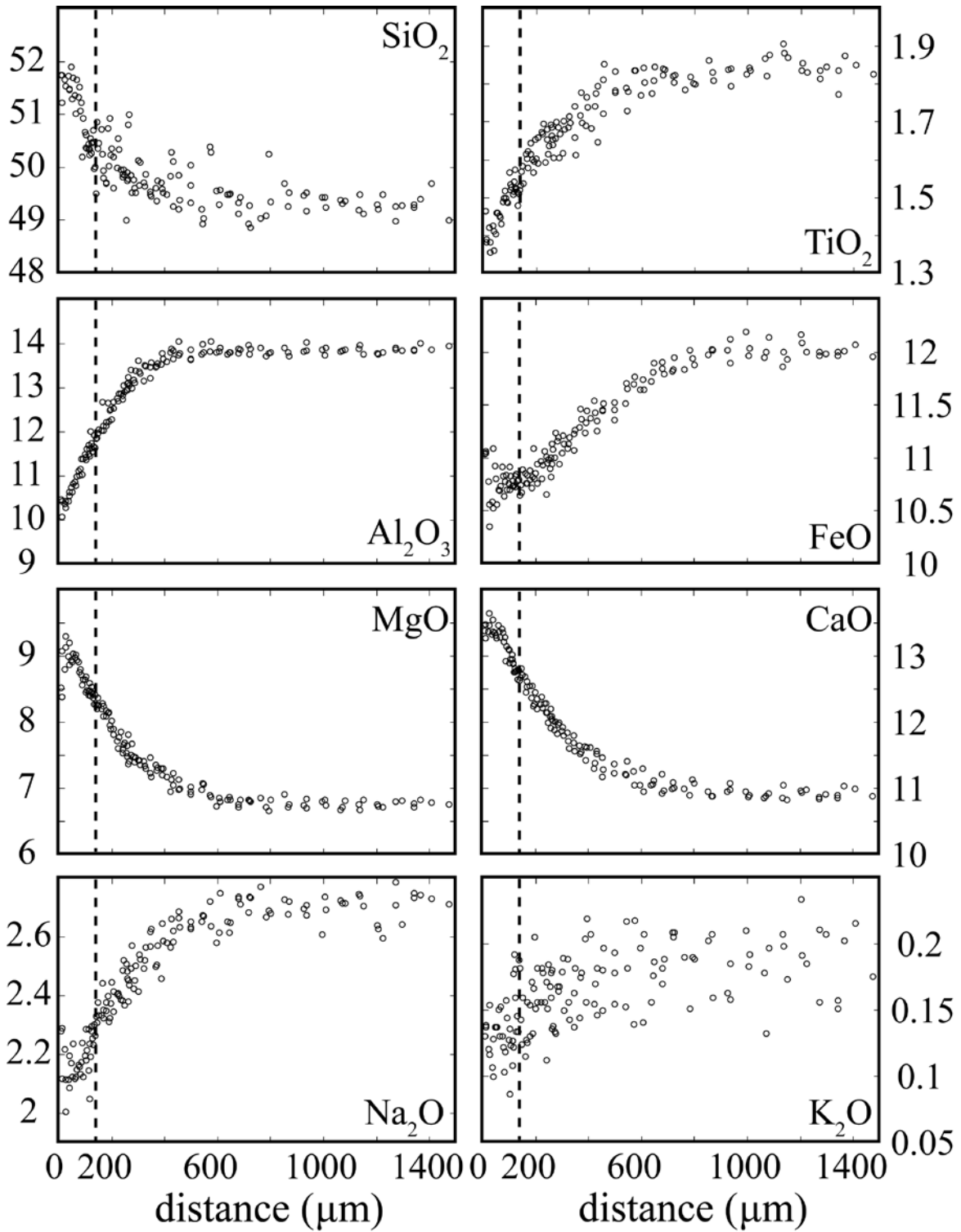


Figure A5. Compositional profiles of Exp#11 (1695 K, 1.90 GPa, 6 minutes). The vertical axes are oxide concentrations in wt%. The horizontal axis is the distance to the clinopyroxene-glass interface. Maximum extent of the quench crystals is marked by the dashed vertical lines.

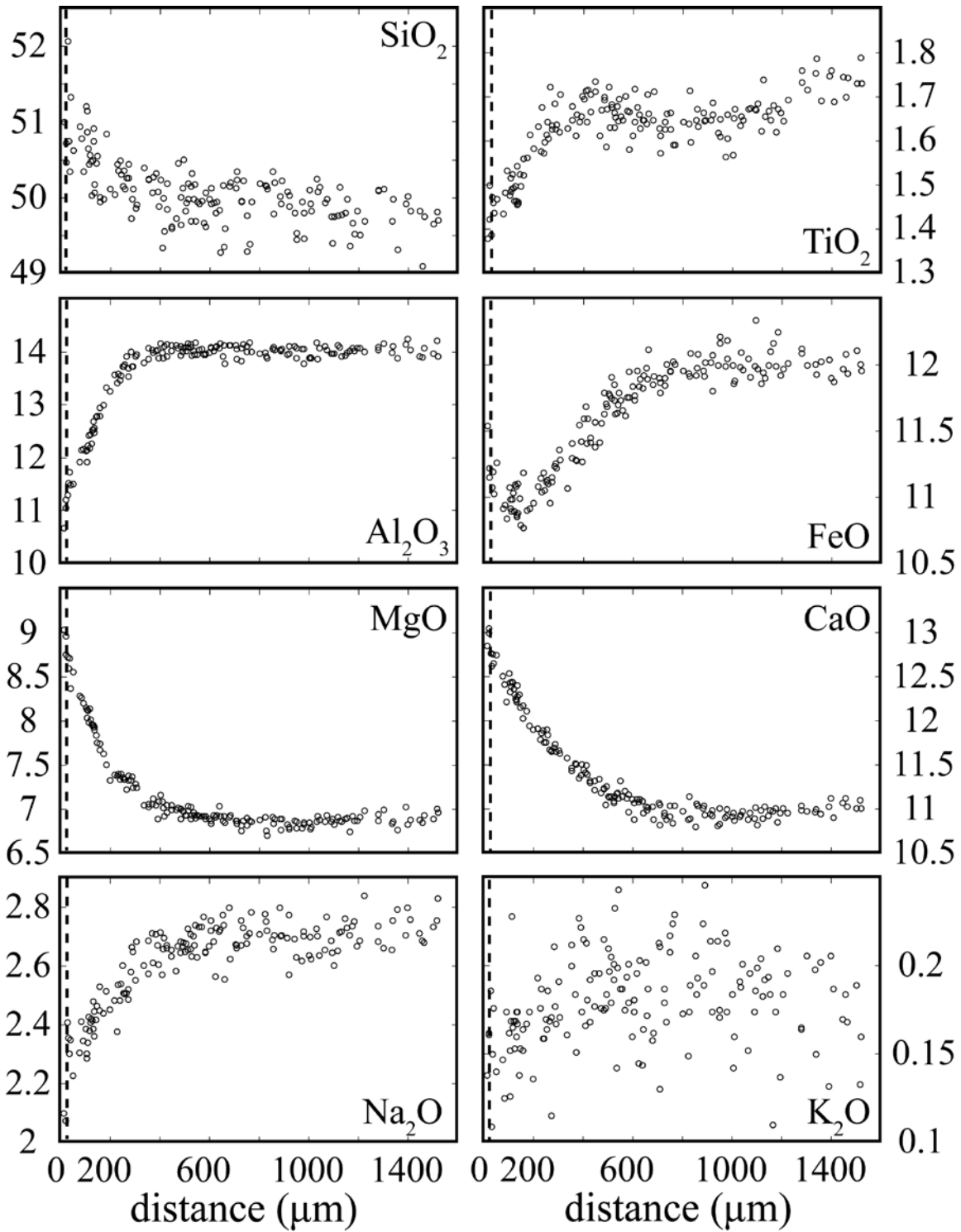


Figure A6. Compositional profiles of Exp#12 (1641 K, 1.42 GPa, 12 minutes). The vertical axes are oxide concentrations in wt%. The horizontal axis is the distance to the clinopyroxene-glass interface. Maximum extent of the quench crystals is marked by the dashed vertical lines.

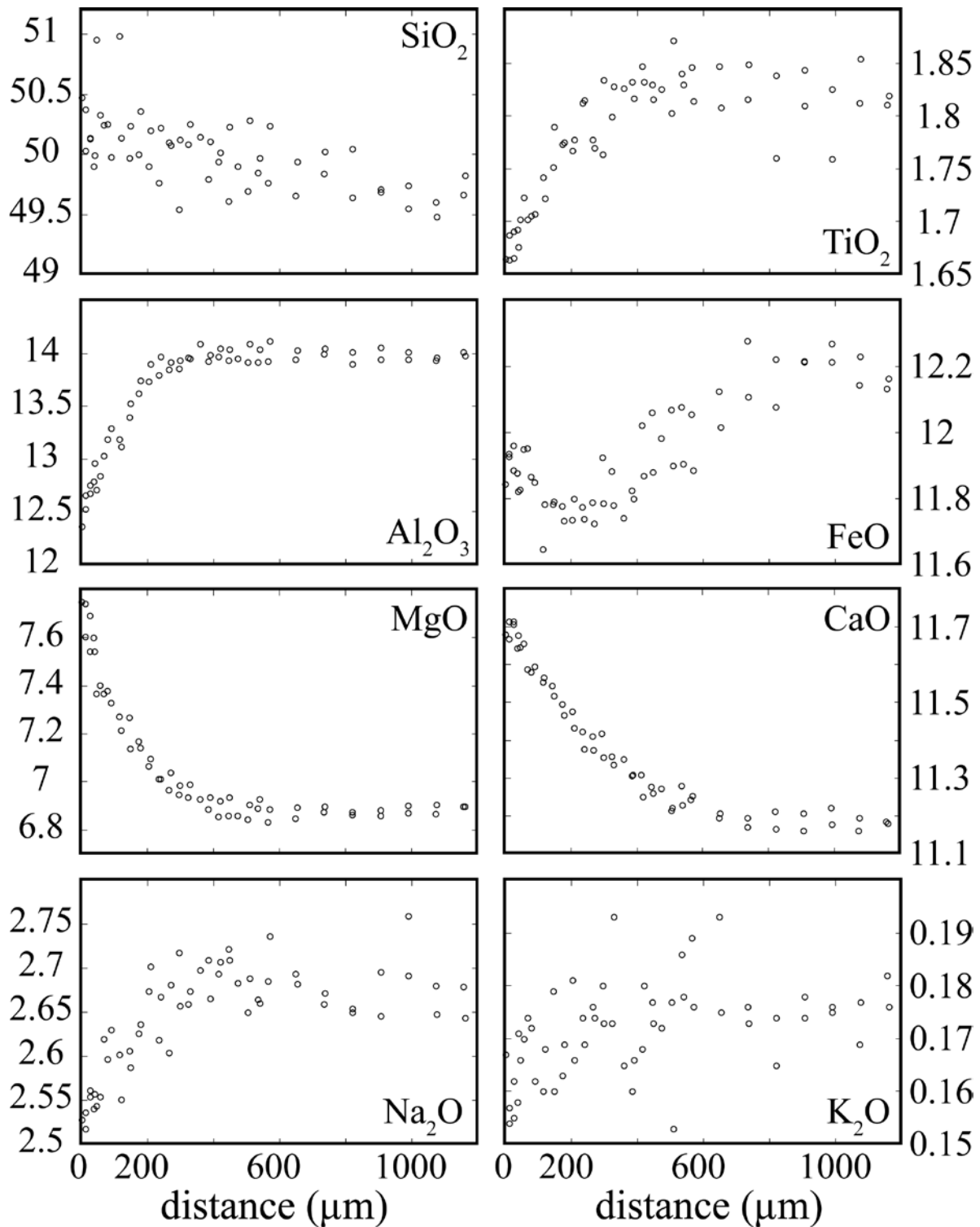


Figure A7. Compositional profiles of Exp#14 (1509 K, 0.47 GPa, 40 minutes). The vertical axes are oxide concentrations in wt%. The horizontal axis is the distance to the clinopyroxene-glass interface. Maximum extent of the quench crystals is marked by the dashed vertical lines.

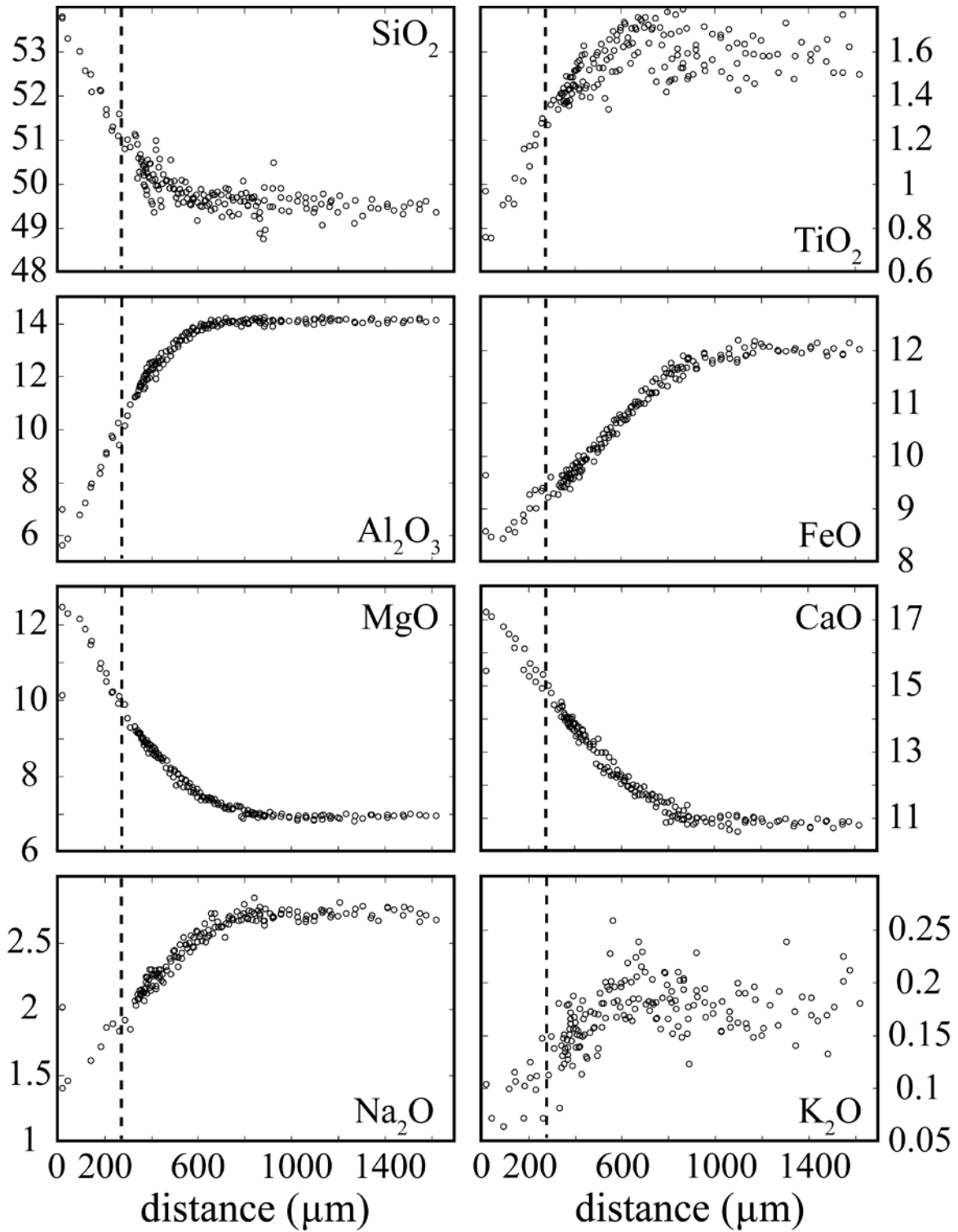


Figure A8. Compositional profiles of Exp#15 (1790 K, 1.90 GPa, 5 minutes). The vertical axes are oxide concentrations in wt%. The horizontal axis is the distance to the clinopyroxene-glass interface. Maximum extent of the quench crystals is marked by the dashed vertical lines.

Fittings to the compositional profiles

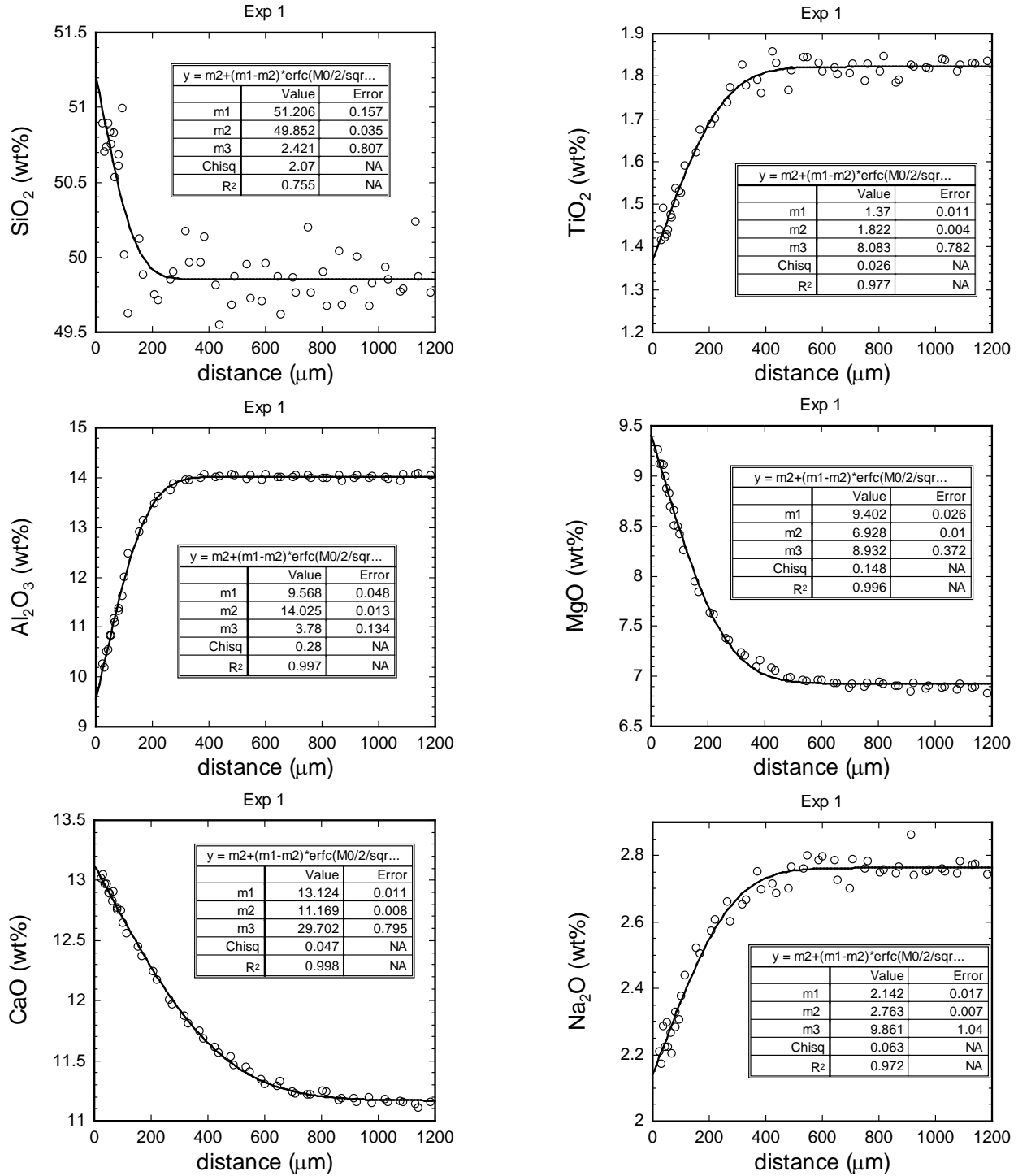


Figure A9. Fittings to the compositional profiles of Exp#1. In the legend of the fitting, m1 is the interface concentration (wt%), m2 is the far-field concentration (wt%), and m3 is the diffusivity (μm<sup>2</sup>/s).

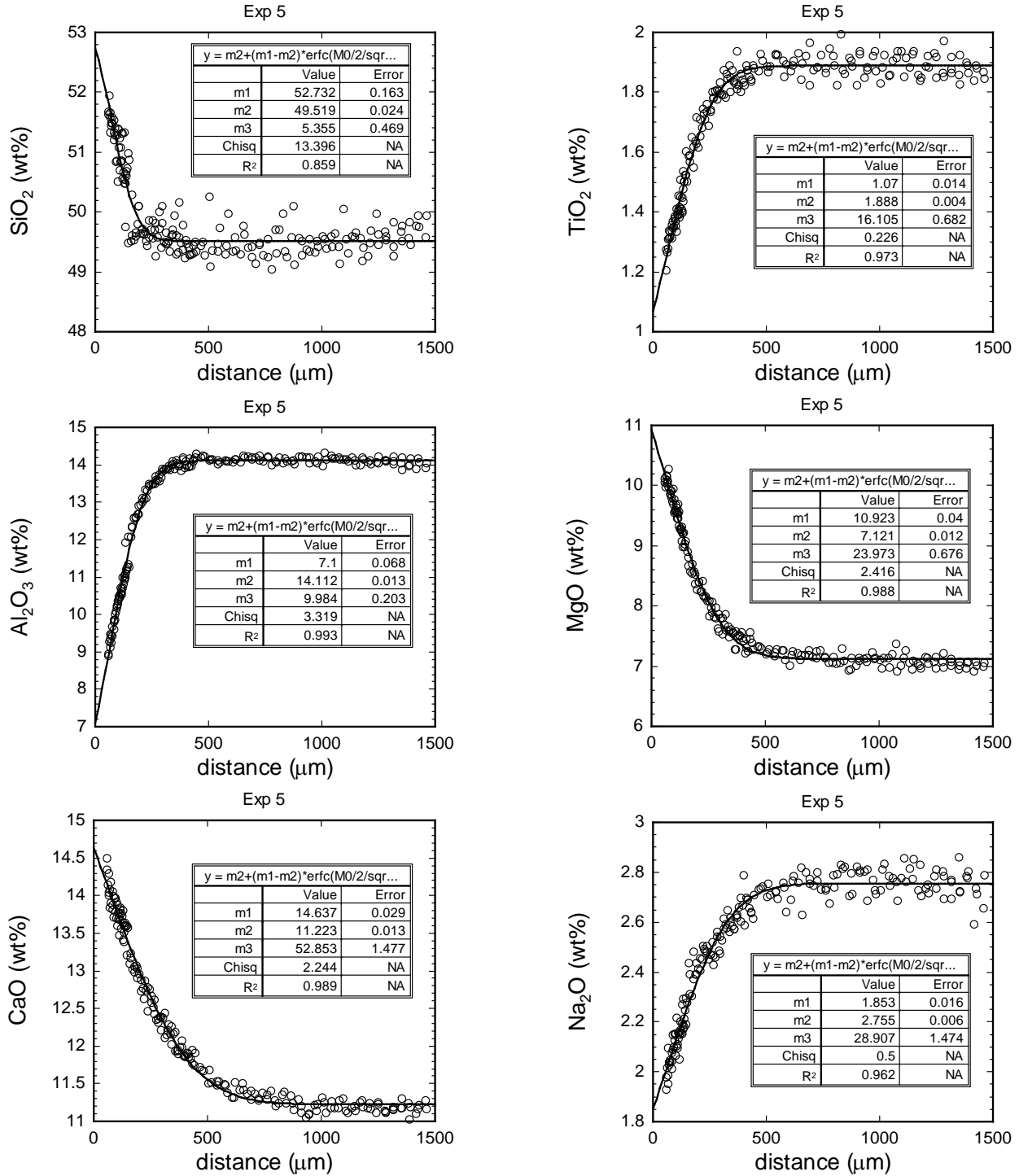


Figure A10. Fittings to the compositional profiles of Exp#5. In the legend of the fitting, m1 is the interface concentration (wt%), m2 is the far-field concentration (wt%), and m3 is the diffusivity (μm<sup>2</sup>/s).

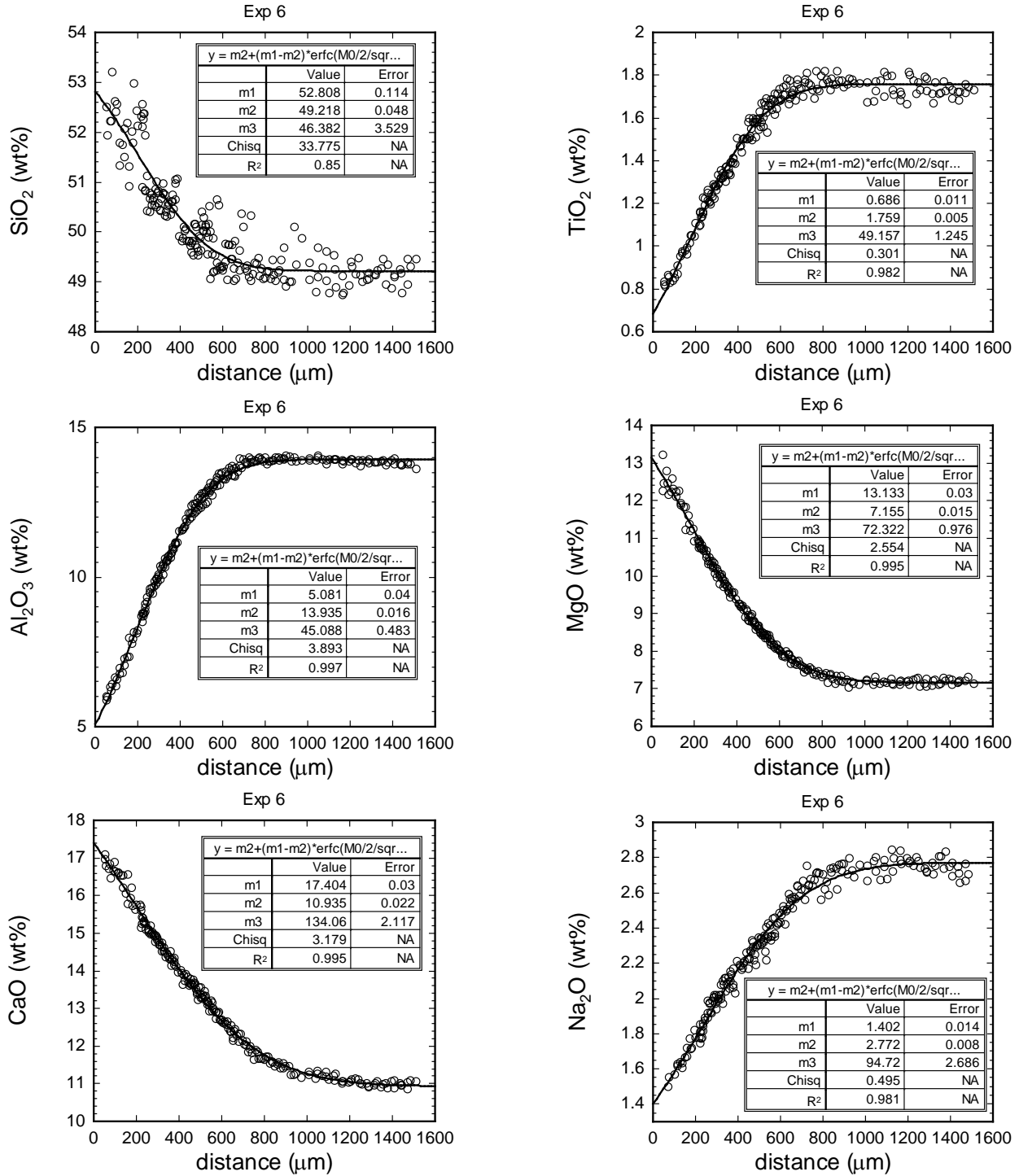


Figure A11. Fittings to the compositional profiles of Exp#6. In the legend of the fitting, m1 is the interface concentration (wt%), m2 is the far-field concentration (wt%), and m3 is the diffusivity ( $\mu\text{m}^2/\text{s}$ ).

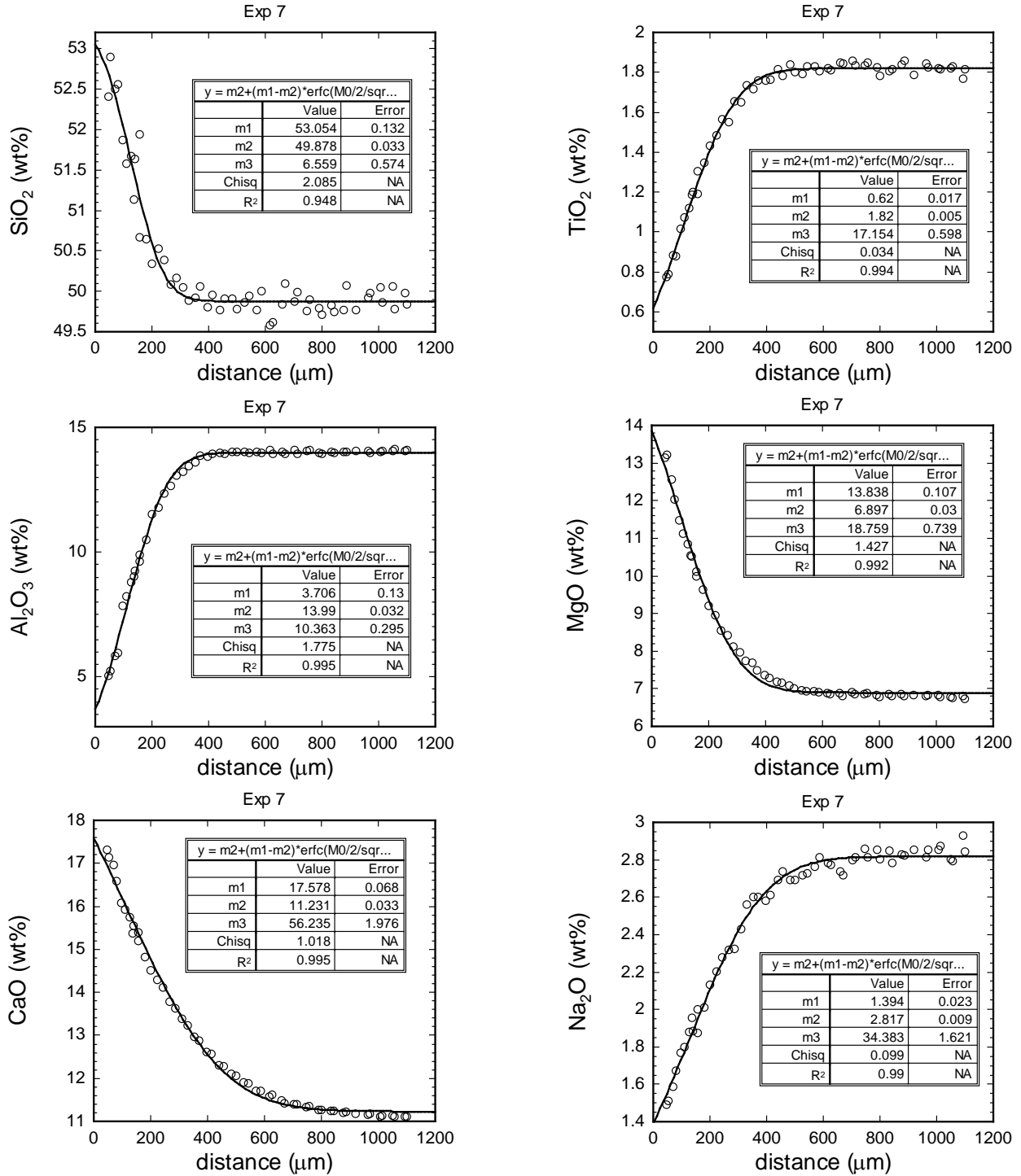


Figure A12. Fittings to the compositional profiles of Exp#7. In the legend of the fitting, m1 is the interface concentration (wt%), m2 is the far-field concentration (wt%), and m3 is the diffusivity ( $\mu\text{m}^2/\text{s}$ ).

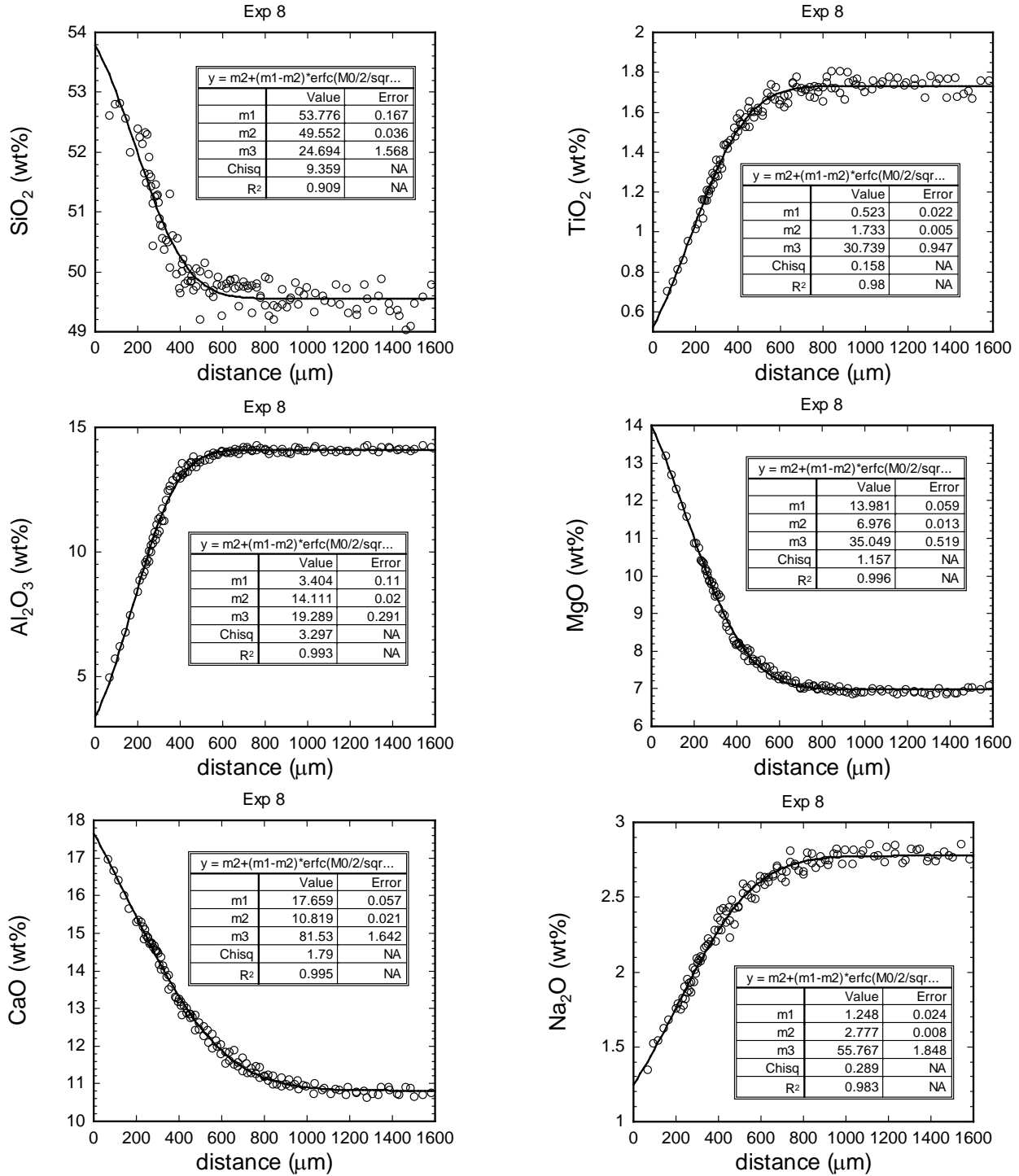


Figure A13. Fittings to the compositional profiles of Exp#8. In the legend of the fitting, m1 is the interface concentration (wt%), m2 is the far-field concentration (wt%), and m3 is the diffusivity ( $\mu\text{m}^2/\text{s}$ ).

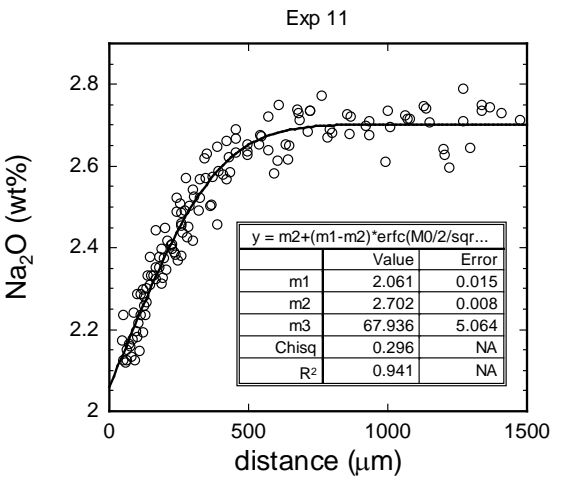
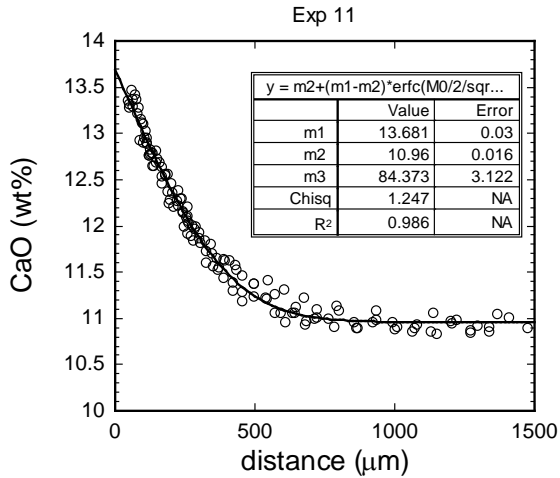
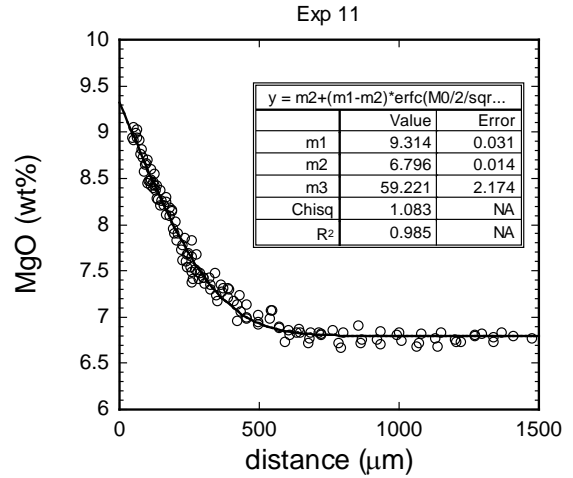
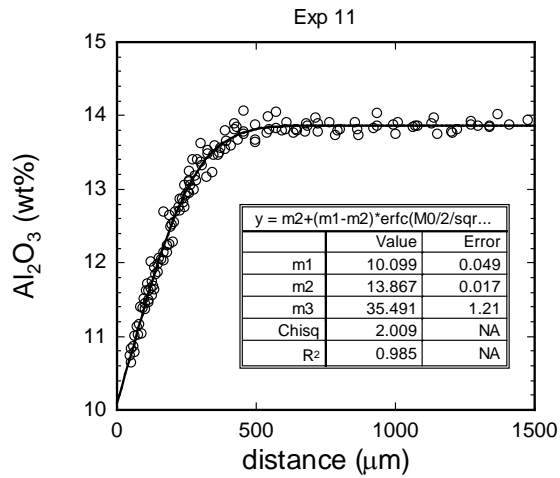
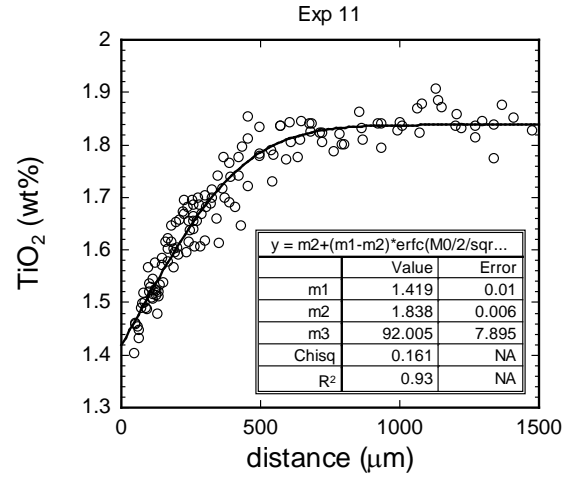
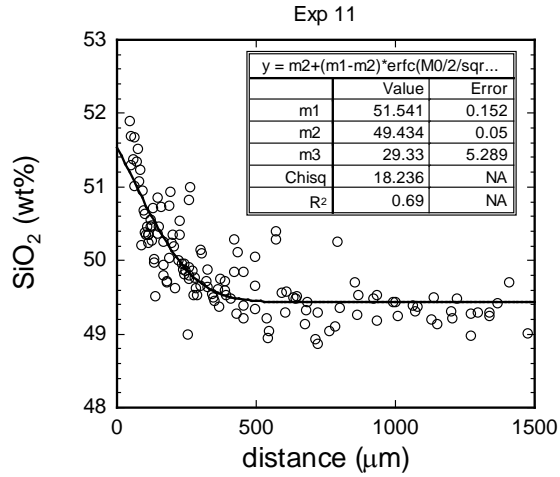


Figure A14. Fittings to the compositional profiles of Exp#11. In the legend of the fitting, m1 is the interface concentration (wt%), m2 is the far-field concentration (wt%), and m3 is the diffusivity ( $\mu\text{m}^2/\text{s}$ ).

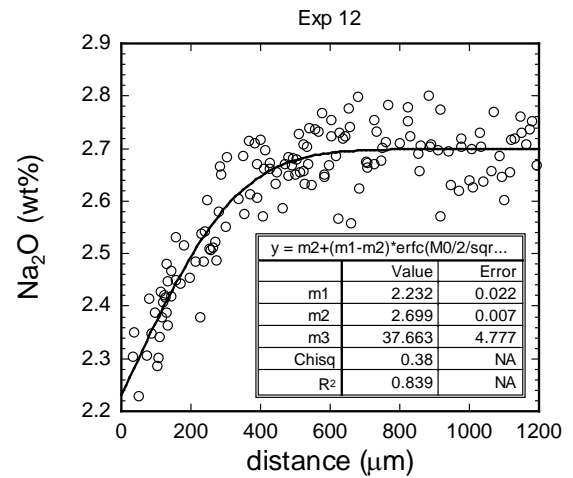
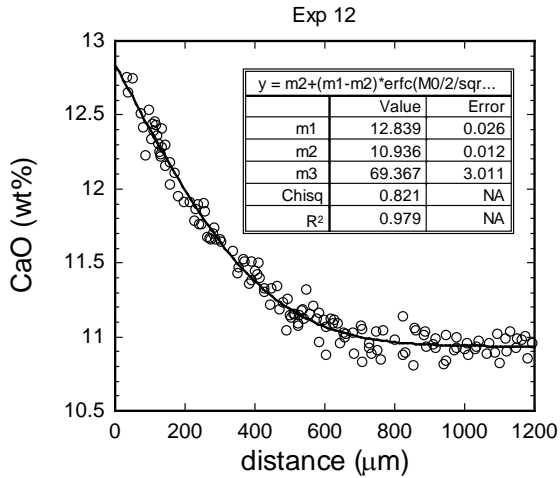
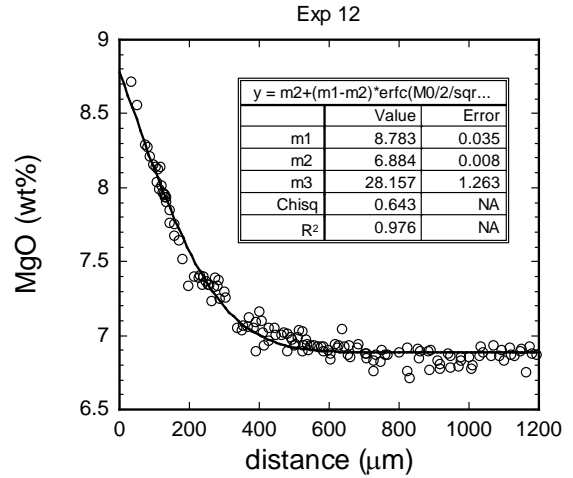
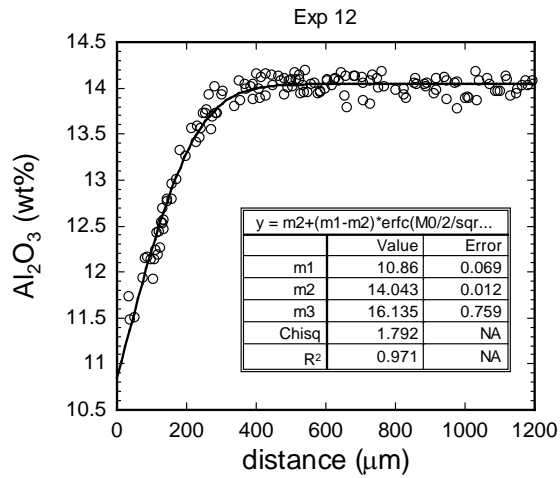
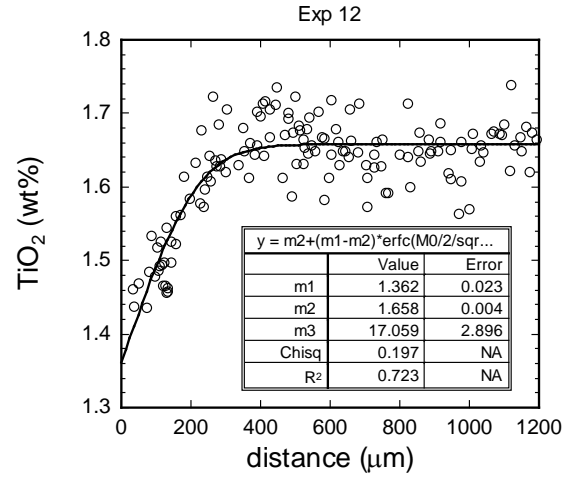
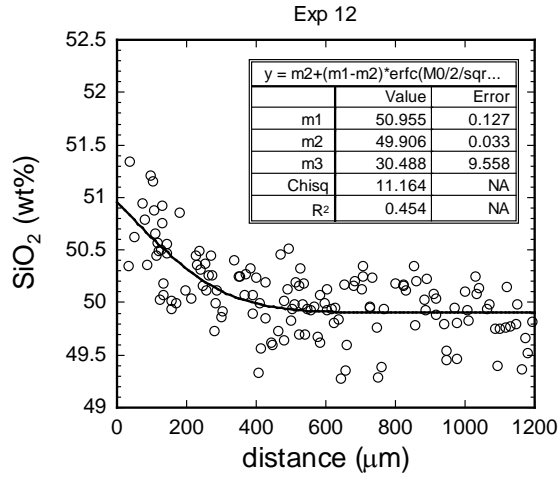


Figure A15. Fittings to the compositional profiles of Exp#12. In the legend of the fitting, m1 is the interface concentration (wt%), m2 is the far-field concentration (wt%), and m3 is the diffusivity ( $\mu\text{m}^2/\text{s}$ ).

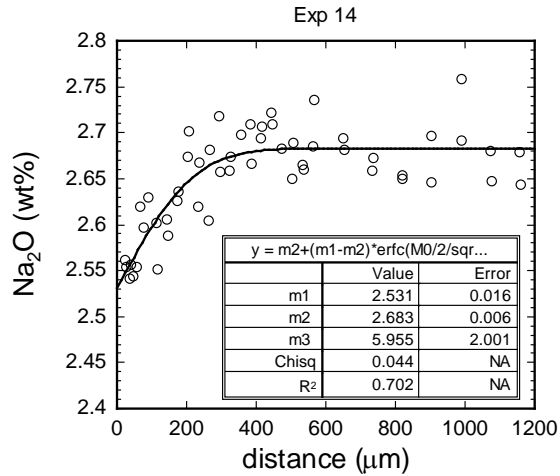
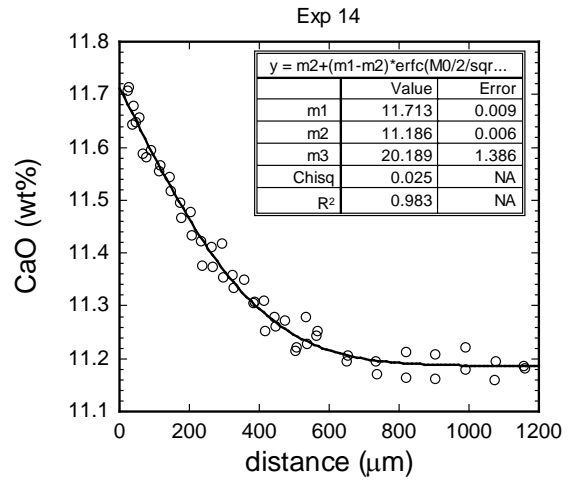
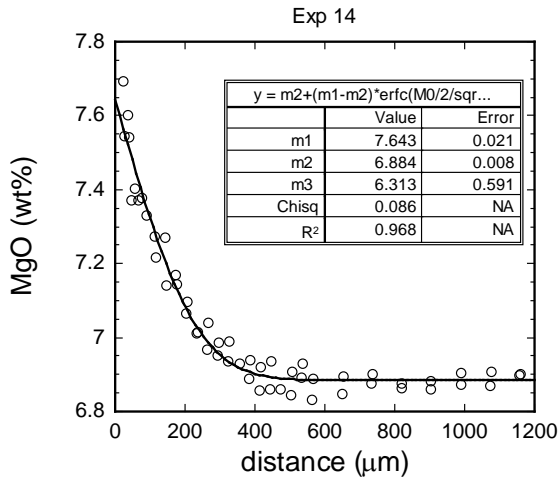
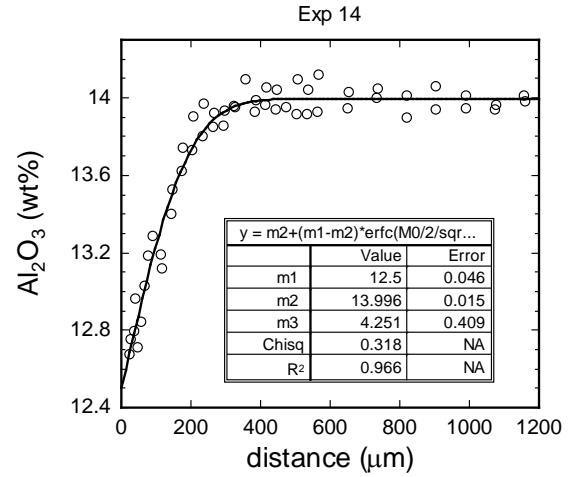
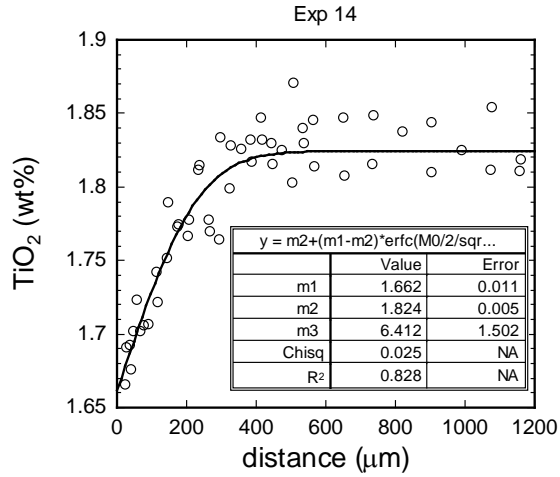


Figure A16. Fittings to the compositional profiles of Exp#14. In the legend of the fitting, m1 is the interface concentration (wt%), m2 is the far-field concentration (wt%), and m3 is the diffusivity ( $\mu\text{m}^2/\text{s}$ ).

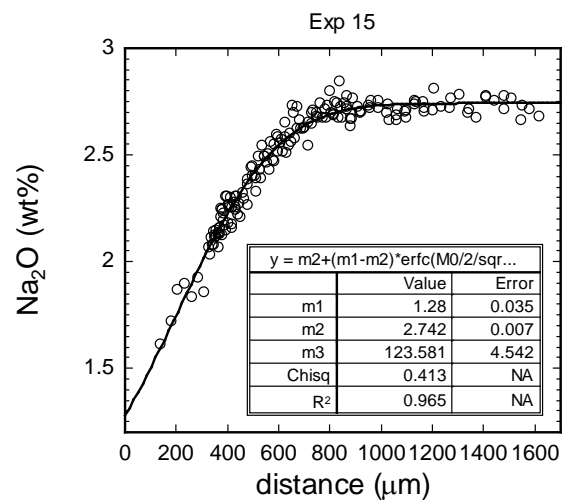
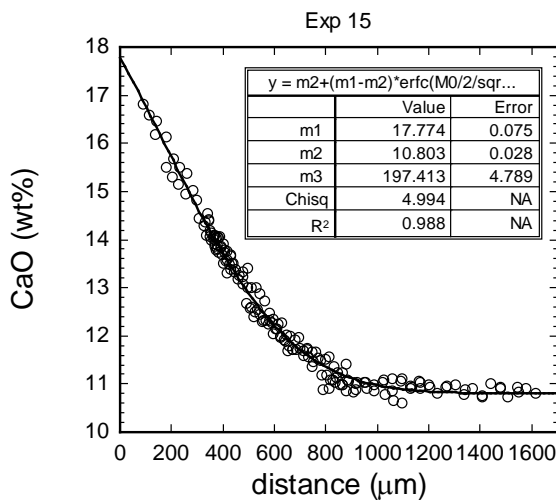
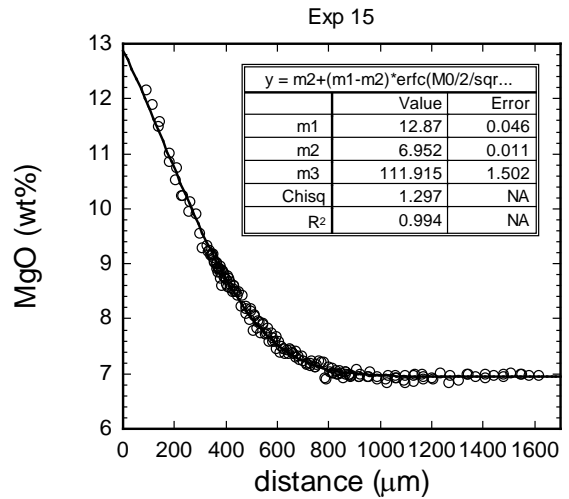
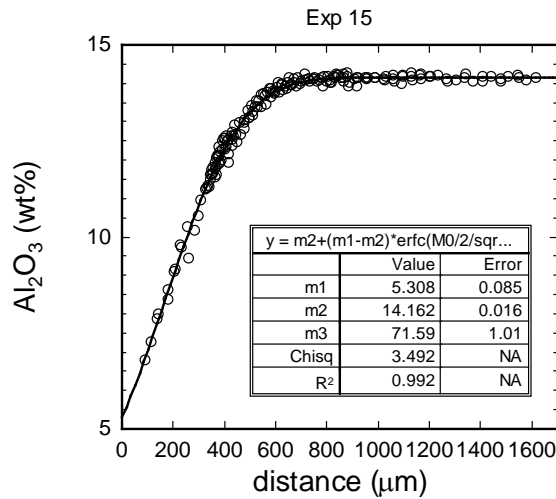
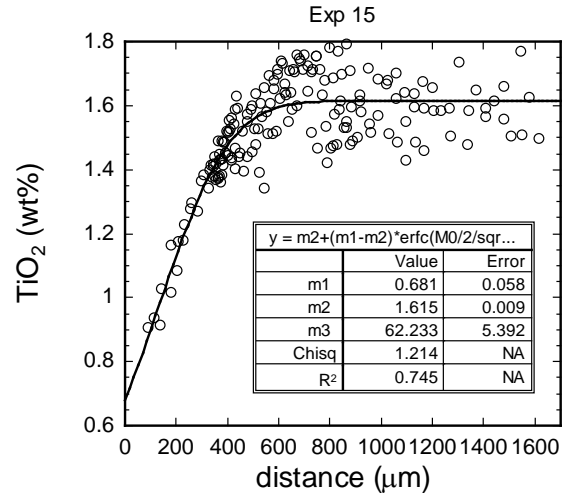
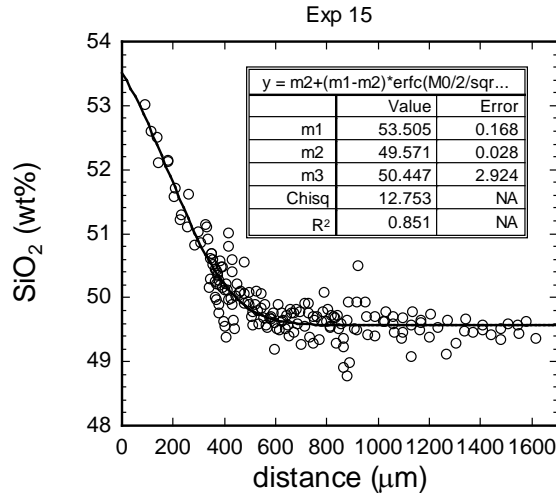


Figure A17. Fittings to the compositional profiles of Exp#15. In the legend of the fitting, m1 is the interface concentration (wt%), m2 is the far-field concentration (wt%), and m3 is the diffusivity ( $\mu\text{m}^2/\text{s}$ ).

## Far-field melt compositions

Table A1. Far-field melt compositions<sup>a</sup> with  $2\sigma$  fitting errors (wt%)

Exp#	SiO <sub>2</sub>		TiO <sub>2</sub>		Al <sub>2</sub> O <sub>3</sub>		FeO <sup>b</sup>		MgO		CaO		Na <sub>2</sub> O	
1	49.85 <sup>c</sup>		1.82	0.01	14.03	0.03	12.0	6.93	0.02	11.17	0.02	2.76	0.01	
5	49.52	0.05	1.89	0.01	14.11	0.03	12.0	7.12	0.02	11.22	0.03	2.76	0.01	
6	49.22	0.10	1.76	0.01	13.94	0.03	12.0	7.16	0.03	10.93	0.04	2.77	0.02	
7	49.88	0.07	1.82	0.01	13.99	0.06	12.0	6.90	0.06	11.23	0.07	2.82	0.02	
8	49.55	0.07	1.73	0.01	14.11	0.04	12.0	6.98	0.03	10.82	0.04	2.78	0.02	
11	49.43	0.10	1.84	0.01	13.87	0.03	12.0	6.80	0.03	10.96	0.03	2.70	0.02	
12	49.91 <sup>c</sup>		1.66	0.01	14.04	0.02	12.0	6.88	0.02	10.94	0.02	2.70	0.01	
14	49.70 <sup>c</sup>		1.82	0.01	14.00	0.03	12.1	6.88	0.02	11.19	0.01	2.68	0.01	
15	49.57	0.06	1.62	0.02	14.16	0.03	12.1	6.95	0.02	10.80	0.06	2.74	0.01	

a: MnO is ~0.2 wt%, K<sub>2</sub>O and P<sub>2</sub>O<sub>5</sub> are ~0.1 wt%.

b: FeO profiles are not fitted. The far-field FeO concentrations are approximately estimated.

c: SiO<sub>2</sub> profiles of these experiments were not treated. The SiO<sub>2</sub> concentrations are estimated.